International Journal of Multiphase Flow 34 (2008) 829–851

Contents lists available at ScienceDirect

International Journal of Multiphase Flow

journal homepage: www.elsevier.com/locate/ijmulflow

Active manipulation of a particle-laden jet

D.A. Tamburello, M. Amitay *

Mechanical, Aerospace, and Nuclear Engineering Department, Rensselaer Polytechnic Institute, Troy, NY 12180, USA

ARTICLE INFO

Article history:
Received 23 September 2007
Received in revised form 19 December 2007
Available online 10 March 2008

Keywords:
Synthetic jets
Flow control
Preferential concentration
Particle-laden jet
PTV

ABSTRACT

The interaction of a particle-laden jet ($Re_{U_e} = 6600$) with a single synthetic jet or a continuous control jet located upstream of the main jet exit (i.e., within the main jet nozzle) was examined experimentally using PIV and PTV. A reduction technique was used to calculate 3-D flow fields from multiple 2-D measurement planes to study the complex 3-D interactions. The synthetic jet was shown to influence the particles both directly and indirectly through the manipulation of the carrier fluid's drag force on the particles. The synthetic jet impulse *directly* vectors the particles away from the synthetic jet, while the formation of large vortical structures *indirectly* affects the particles, spreading throughout the measurement domain. By comparison, a continuous control jet only vectors the particles away from itself. The lowest Stokes number particles respond similarly to the carrier fluid, while higher Stokes number particles are less responsive to the control and only follow the strong vortical structures (i.e., higher circulation), which suggests that the preferential concentration concept depends on both the Stokes number as well as the strength of the coherent structures.

1. Introduction

Active flow control of a single-phase jet has been a topic of research over the last few decades (Yule, 1978). Adding a discrete phase to a fluid, such as solid or liquid particles or bubbles, adds a level of complexity due to both the interactions between the discrete phase and the carrier fluid as well as the response of the particles to control. These multiphase flows are of immense interest as they can be found in a variety of engineering applications, including internal combustion engines, liquid and solid propellant rockets, cyclone combustors, biomass gasifiers, dental caries removal, sand-blasting, and many others.

Many studies have been conducted to examine the effects of flow control on particle-laden flows, where the main focus was to alter the fluid flow field characteristics, such as the vortical structures, turbulence quantities, mixing characteristics, or mean velocity profiles, and, thus, affect the particulate phase indirectly. However, unlike single-phase flows, multiphase flows pose a new difficulty in the presence of the second phase that can, and usually does, alter any or all of the flow field characteristics. The lack of accurate, predictive models of the effects of various flow control techniques on the particulate and fluid phases in tandem with more accurate methods of experimental investigations of these flows have produced an increase in the research related to the control of particle-laden flows in recent years.

An important concept related to indirect particle-laden flow control is *preferential concentration* (Eaton and Fessler, 1994; Fessler et al., 1994; and others), which describes the accumulation of particles within specific regions of a turbulence field. This is driven by two mechanisms: centrifuging of particles away from vortical structures and accumulation of particle clusters in highly strained convergence zones with low vorticity. Preferential concentration is strongest for Stokes numbers of order one, where the particle time scales match the vortex motions that actually cause the concentrations (Eaton and Fessler, 1994). Numerous experimental and numerical studies have demonstrated the effects of preferential concentration for many types of flows, for example, isotropic turbulence (Squires and Eaton, 1990, 1991; Wood et al., 2005), backward facing steps (Fessler and Eaton, 1997; Glezer and Amitay, 2002; Yu et al., 2004), plane wakes (Yang et al., 2000), and duct flows (Winkler et al., 2004). For axisymmetric jets, the more important effect of preferential concentration appears to be the formation of particle clusters in the highly strained regions of low vorticity, with the jet showing great sensitivity to the initial particle location (Eaton and Fessler, 1994).

One of the most commonly used methods of active flow control is to acoustically excite the particle-laden flow using a speaker in the jet's plenum (e.g., Longmire and Eaton, 1992, 1994; Anderson and Longmire, 1995; Sakakibara et al., 1996; Hoffmann and Moreira, 1996; Anderson, 1997; Cerecedo et al., 2004; and others). Longmire and Eaton (1992) demonstrated that, in the presence of acoustic excitation, particle dispersion was dominated by convection via coherent structures (vortex rings) rather than by diffusion due to random three-dimensional turbulence. In areas with large

* Corresponding author. Tel.: +1 518 276 3340.
E-mail address: amitam@rpi.edu (M. Amitay).

0301-9322/$ - see front matter © 2008 Elsevier Ltd. All rights reserved.
doi:10.1016/j.ijmultiphaseflow.2008.02.006

vortical structures, the jet contained distinct regions of high and low particle concentration corresponding to highly strained regions of low vorticity (between vortex rings) and areas of high vorticity (the vortex rings themselves), respectively. Moreover, a large percentage of particles were ejected away from the jet by the outward moving fluid at these locations of high vorticity. Particles could not follow strongly diverging fluid streamlines nor decelerate as quickly as the fluid phase, which explains why particles were ejected by vortical structures rather than entrained back into the jet (Anderson and Longmire, 1995; Sakakibara et al., 1996; Anderson, 1997).

In a later work, Longmire and Eaton (1994) showed that the formation of high particle density clusters and the delay of strong particle dispersion can be accomplished when the excitation waveform consisted of two frequencies, a fundamental and a sub-harmonic, rather than a single frequency. This concept was confirmed by Kiger and Lasheras (1995, on a shear layer) as well as Cerecedo et al. (2004, on an axisymmetric jet). Furthermore, additional control of the vortex pairing location as well as the nature of cluster merging and subsequent dispersion can be accomplished by varying the phase between the two forcing waves (Longmire and Eaton, 1994). Hoffmann and Moreira (1996) noted that the carrier fluid boundary conditions also played a prominent role in controlling particle ejection (from vortical structures) and clustering. In addition, larger particles (higher τ_p) had higher particle/fluid correlations due to the differences in the turbulence field (Sakakibara et al., 1996).

Another time-periodic excitation method, using an oscillating wall section, showed that the actuation affected particle velocity and distribution both directly, by altering the boundary conditions seen by the particles through wall impact, and indirectly, by controlling the spacing and size of coherent vortices in the jet (Pothos, 2002; Pothos and Longmire, 2002). The direct effects required a significant impact velocity and wall displacement and were useful for reducing high particle concentration layers evolving near the channel sidewalls at their rectangular jet's exit. The indirect effects, which were associated with the lowest Strouhal numbers (largest vortices) and the smallest particles, were similar to those using a speaker in the jet's plenum as described above.

Another common method of particle-laden flow control is adding a swirl to the jet (e.g., Bulzan et al., 1987; Amitay et al., 2003; Apte et al., 2003; and others). Adding swirl results in an increase in particle spreading rates and the concentration of particles into a hollow-cone pattern along the outside edge of the jet due to centrifugal forces. Amitay et al. (2003) showed that the particles did not follow (move slower than) the carrier fluid and were ejected from the swirling fluid, thus explaining the large spreading rates and hollow-cone patterns. Yu et al. (2003) showed similar results in their numerical simulation of a pipe flow, with particles being ejected from the centerline toward the pipe walls and a strong dependence on the particle size.

In some cases, passive forms of flow control have been used. Middha and Wexler (2003) redesigned a focusing nozzle (similar to those used in aerosol sprays) using additional structures within the nozzle upstream of the exit to improve particle concentration and trajectories. Particles near the boundary layer did not undergo the same acceleration as those in the jet core and, thus, were not easily influenced by the sharp turns and quick decelerations within the nozzle. In addition, particles with Stokes numbers on the order of one were the most responsive to changes in the nozzle.

In other investigations, multiple flow control methods were used (Wicker and Eaton, 1999, 2001). When acoustic excitation was combined with swirl, Wicker and Eaton (2001) showed an increase in radial particle dispersion due to the large vortex structures. The acoustic excitation preferentially concentrated the particles into relatively narrow bands with concentration peaks occurring in the saddle regions between vortex rings. These rings play a strong role in preferential concentration, even in a highly turbulent swirling jet field, as they more effectively disperse the particles and cause directed particle motions.

Wicker and Eaton (1999) also added large three-dimensional perturbations, in the form of four equally spaced vortex generators, to the acoustically-excited swirling jet to significantly alter the particulate and fluid structures. The passive vortex generators added longitudinal vorticity (at an opposite sign from the swirl) and disrupted the development of the axial vortex rings, thereby reducing radial particle dispersion and particle flinging. Vortex generators also altered the signature of the particle concentration field making it azimuthally asymmetric. Preferential particle concentrations remained, but the large-scale structures did not appear to significantly increase the radial particle dispersion. The initial asymmetry in the axial structure, due to the injected longitudinal vorticity, was sufficient to disrupt the effectiveness of the vortex rings to disperse particles radially. Thus, the ability of the vortex generators to reduce particle flinging by vortex rings may be important in practical applications.

To the best of the authors' knowledge, synthetic jet actuators (e.g., Smith and Glezer, 1998, 2002; Glezer and Amitay, 2002; Amitay and Cannelle, 2006; and others) have never been implemented with particle-laden jets. A review of this technology, including many of its application, is provided by Glezer and Amitay (2002). The synthetic jet actuator is unique among fluidic control methods because it is synthesized from the working fluid of the flow system. Thus, it transfers momentum to the flow with no net mass injection across the flow boundary while eliminating the need for an additional fluid source and extraneous pumping and piping (Smith and Glezer, 1998, 2002; Cannelle and Amitay, 2005; Amitay and Cannelle, 2006).

The motivation of the present paper is to explore, experimentally, the direct and indirect particle flow control mechanisms associated with the use of a single synthetic jet actuator mounted perpendicular to an axisymmetric particle-laden jet. In particular, the authors seek to explore the resulting three-dimensional flow field as well as to get a better understanding of the mechanisms associated with the activation of the synthetic jet. Another objective is to examine the weighted contribution of each mechanism by comparing the effects of the synthetic jet with those found using a continuous control jet as well as by changing the synthetic jet's upstream location (i.e., within the main jet nozzle). The goal of this paper is to enhance the current knowledge of particle-laden flows to improve the effectiveness of flow control for particle concentration, vectoring, and spreading. Furthermore, understanding the effect of a single synthetic jet is the first step in understanding the effect of multiple control jets.

2. Experimental facility

Using the same jet assembly as the previous work of Tamburello and Amitay (2007a), an experimental investigation was conducted in a $1.56 \times 0.72 \times 0.72$ m clear-walled enclosure using a LaVision particle image velocimetry (PIV) system, with particle tracking velocimetry (PTV) capabilities. The PIV system consists of a double-pulsed, Nd:Yag laser, a high resolution CCD camera, and a programmable timing unit. The laser beam was transformed into a sheet using a cylindrical lens and was focused through an optical lens to create a light sheet approximately 1 mm thick at the center of the measurement domain. The repetition rate was selected so it will not bias the data; this was accomplished by ensuring that it was not a sub-multiple of either the actuation frequency or the natural frequencies of the flow. For more information on the experimental setup, see Tamburello (2007).

For the current investigation, the single-phase velocity vectors were calculated using a cross-correlation PIV technique with adaptive multi-pass and deformable interrogation windows with 50% overlap. For the majority of the data, a single pass at 64 × 64 followed by two passes at 32 × 32 pixels was used to calculate the velocity vectors. The camera was mounted at a perpendicular distance of ~0.4 m to the laser light sheet such that the distance between pixels is ~27.1 μm, with a maximum flow tracer displacement of approximately 7 pixels resulting in an error of approximately ±0.1 pixels (±0.37 m/s).

For the particle-phase, a PTV method based on the size and intensity values of the particles was used to identify particles and to calculate their velocities and concentration. If a potential particle (two matched correlation peaks from the two image exposures) matched specific pixel size and intensity criteria, it was identified as a particle and its velocity was calculated. All valid particles were then counted at a given position (using their centroids) over the set of images to calculate their concentrations. For the majority of the data presented, the particles were examined independently, without the use of flow tracers for the gaseous phase. This is discussed later in the text. In addition, to minimize the resulting file size and processing time, the particle fields are converted from the pixel-by-pixel resolution at which the data were acquired to a 4 × 4 pixel grid (i.e., averaged over a 4 × 4 pixel interrogation domain) with a maximum loss of less than 0.1% of the total number of particles during the conversion.

Spherical, titanium dioxide particles with a nominal diameter of 0.3 μm were used as flow tracers for the single phase jet measurements and flow visualization. The particles used in this study were solid glass spheres with a nominal density of approximately 2.5 g/cc. A summary of the characteristics for each particle class can be found in Table 1. The particles, which will be referred to as *T*01, *T*09, and *T*19 based on their particle response times defined by Eq. (2.1), are centered at diameters, $d_{p,ave}$, of 11 μm, 35 μm, and 50 μm, respectively.

$$\tau_p = \frac{\rho_p d_p^2}{18\mu} \tag{2.1}$$

Here, τ_p is the particle response time, ρ_p is the particle density, d_p is the particle diameter, and μ is the carrier fluid viscosity. The values of τ_p are approximately 19, 9, and 1 for the *T*19, *T*09, and *T*01 particles, respectively. However, because these particles have Reynolds numbers, Re_p, greater than unity, the assumptions of Stokes' analysis no longer hold (Eaton and Fessler, 1994). Thus, for higher particle Reynolds numbers, the adjusted particle response time, τ_p^*, can be estimated using relatively simple drag laws ($Re_p \leqslant 700$ for Torobin and Gauvin, 1959; Fessler et al., 1994) such as Eq. (2.2):

$$\tau_p^* = \frac{\tau_p}{1 + 0.15 Re_p^{0.687}} \tag{2.2}$$

Here, Re_p is the particle Reynolds number and is defined by Eq. (2.3), where ν is the fluid kinematic viscosity, U is the carrier fluid velocity, and U_p is the particle velocity:

$$Re_p = \frac{(U - U_p) d_p}{\nu}. \tag{2.3}$$

For the current work, the particle Reynolds number is calculated along the main jet centerline at $x/d_e = 0.5$.

The most common definition for the fluid characteristic time scale (τ_f) of an axisymmetric free jet (Hardalupas et al., 1989; Eaton and Fessler, 1994; Hoffmann and Moreira, 1996; Amitay et al., 2003; Middha and Wexler, 2003; and others) is defined as the ratio of the main jet exit diameter, d_e, to the carrier fluid exit velocity, U_e. However, for the current work, the fluid flow is forced using periodic excitation, which provides a more appropriate fluid time scale based on the frequency of the excitation, f, as shown in Eq. (2.4):

$$\tau_f = \frac{1}{f} \tag{2.4}$$

The Stokes number, *St*, which is the ratio of the particle response time to the carrier fluid characteristic time scale, was then calculated. Note that Table 1 provides three different Stokes number calculations (based on Eqs. (2.1), (2.2) and (2.4)) for each of the particle classes, with the last entry, $St^*_{f,25m/s}$, being the most appropriate for particle categorization.

Both flow tracers and particles were introduced upstream of the nozzle assembly using air-based atomizers. By controlling the pressure in the atomizers, a particle (or tracer) flow rate could be produced. In addition, by adding the particles (and/or tracers) upstream of the nozzle assembly (rather than within it), the particles (and/or tracers) remain more evenly distributed throughout each sequence of images. The gas flow rate was kept constant for each case using a flow meter (Top-Trak Mass Flow Meter model Sierra 826-NX-OVI-PV1-V1-MP) with a maximum volumetric flow rate of 100 L/min (~125 m/s for the current nozzle assembly). For more information on the experimental setup, see Tamburello (2007).

A sequence of 500 image pairs was used to calculate the ensemble averages and turbulent quantities for the single-phase jet. Compared to the same values calculated from 2000 image pairs, the 500 image pairs have a difference in the ensemble average and turbulent quantities magnitudes of less than 1% and 10%, respectively, with very similar flow fields. For the *T*01, *T*09, and *T*19 particles, a sequence of 1000, 4000, and 5000 image pairs, respectively, were used to calculate the particle velocities, RMS values, and particle number densities. The number of instantaneous image pairs necessary to describe a full data set was found by comparing these quantities for a given particle size. Note that no data were taken for fewer than three particles at a given location for any of the particle classes.

The gas- and particle-phase accuracies were deemed sufficient since the objective of the present work is to compare the flow fields with and without the activation of the synthetic jet. In addition, this saved significant time and space that is required to acquire, process, and save the data. The instantaneous velocity vectors for the single-phase jet were validated using the RMS of their eight neighboring vectors, where any vector whose magnitude was larger than twice the RMS was replaced by the average velocity of the neighboring vectors. For the particle laden jet velocity vectors, the instantaneous velocity vector fields were validated using a three step process. First, the instantaneous images were processed via PIV to establish the general velocity trends of the flow field. Next, the instantaneous images were processed using PTV to calculate the particle velocity vectors, which were required to be within 60% of the PIV trend data. Finally, a low/high-pass filter was used

Table 1
Summary of particle and flow tracer characteristics

Particle group	*T*01	*T*09	*T*19	Flow tracers
Material	Glass	Glass	Glass	Titanium dioxide
$d_{p,ave}$ (μm)	11	35	50	0.3
$d_{p,range}$ (μm)	(90%) 4–22	(90%) 27–43	(95%) 44–53	(80%) 0.2–0.45
ρ_p (kg/m^3)	2490	2490	2500	4140
$\tau_{p,ave}$ (ms)	0.920	9.31	19.1	0.00114
$\tau_{p,range}$ (ms)	0.122–3.68	5.54–14.1	14.8–21.5	0.0005–0.0026
$St_{25m/s}$	5.75	58.2	119	0.0071
$Re_{p,o}$	2.86	15.2	17.0	Not measured
$\tau^*_{p,ave}$ (ms)	0.703	4.72	9.31	Not measured
$\tau^*_{p,range}$ (ms)	0.160–2.81	2.81–7.15	7.22–10.5	Not measured
$St^*_{25m/s}$	4.39	29.5	58.0	Not measured
τ_f (ms)	1	1	1	1
$St^*_{f,25m/s}$	0.703	4.72	9.31	Not measured

to eliminate those particle velocities that were outside of realistic limitations.

As was mentioned previously, a single synthetic (zero-net-mass-flux) jet issued perpendicular to the main jet was employed to actively control the particle-laden jet. A control module (made from stereolithography), which incorporated a synthetic jet actuator, was attached directly to the jet assembly, as shown in Fig. 1. The synthetic jet was formed as a result of the periodic motion of a piezoelectric disk that was mounted to one of the walls of a sealed cavity having a single 1.2 mm circular opening, the synthetic jet orifice, d_{sj}. In the present work, the main jet Reynolds number is 6600 (U_e = 25 m/s; d_e = 4 mm) and the driving frequency of the synthetic jet, f, is fixed at 1000 Hz. This corresponds to a Strouhal number (St_r) of 0.16, as defined by Eq. (2.5)

$$St_r = \frac{f d_e}{U_e} \tag{2.5}$$

This frequency was selected such that it is within the range of the natural unstable modes of the main jet and, thus, takes advantage of the main jet's naturally amplifying structures. Note that using this frequency yielded the largest effects on a single-phase jet, as was shown by Tamburello and Amitay (in press). The strength of the synthetic jet (relative to the main jet) is quantified using the momentum coefficient, C_μ, defined as

$$C_\mu = \frac{n\bar{I}_j}{\frac{1}{2}\rho U_e^2 d_e^2} \tag{2.6}$$

$\bar{I}_j$ is the time-average synthetic jet momentum per unit length during the outstroke, and is defined as

$$\bar{I}_j = \frac{1}{\tau}\rho d_{sj}^2 \int_0^\tau u_j^2(t)\,dt \tag{2.7}$$

The phase-averaged centerline velocity, $u_j(t)$, at the synthetic jet exit plane was measured using a single hotwire sensor. In the experiments presented in this paper, $0.005 < C_\mu < 0.16$, with a corresponding peak velocity of 8.8–72 m/s.

A LabView code was written to synchronize the programmable timing unit within the PIV system with the actuation cycle of the synthetic jet to acquire phase-locked data. This code generated two signals; the first was the driving signal for the synthetic jet actuator, while the second was a TTL signal at a sub-multiple frequency of the synthetic jet's driving signal, which served as the trigger for the PIV data acquisition. Data were acquired at a given phase by changing the delay between these two signals.

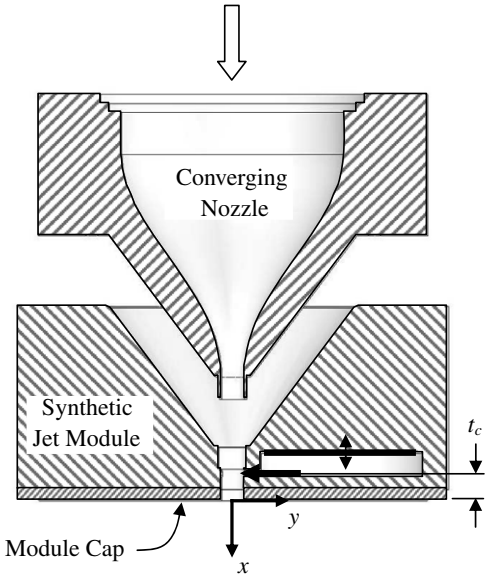

Fig. 1. Schematic of the synthetic jet flow control module.

The single-phase and particle-laden jet flow fields resulting from the interaction with a single synthetic jet actuator are clearly three-dimensional. Thus, a data reduction technique, as outlined by Tamburello and Amitay (2007b,c), based on the work by Schabacker and Bölcs (1996) and Sakakibara et al. (2001), was used that created a three-dimensional measurement grid from multiple two-dimensional measurement planes. This grid does not capture structures smaller than 1 mm; however, it captures the large-scale structures, and this provides valuable insight into the global interactions between the synthetic jet and the main jet. The smaller size structures were explored by analyzing the data at each two-dimensional plane separately, as will be shown later. Note that the synthetic jet was always oriented along the x–y measurement plane along the main jet centerline.

As was shown by Longmire and Eaton (1992), for particle-laden flows with mass loadings less than 11% (or 8% according to Prevost et al., 1996), the particulate phase is assumed to have little to no influence on the fluid phase making simultaneous measurements unnecessary. In addition, Hardalupas et al. (1989) showed that particle-particle interactions were negligible for particle volume fractions lower than 0.3%. Thus, with the mass loading and volume fractions of 1% and 0.0048%, respectively, used in the current study, simultaneous measurement of both phases is unnecessary and particle-particle interactions can be neglected. These assumptions were verified experimentally by taking simultaneous particle/carrier fluid measurements for selected cases. For these simultaneous-measurement cases, high- and low-pass filters were used to remove the particles (high intensity) from the tracers (low intensity). For the tracers, large voids were left by the particles that had been removed, which required additional processing to eliminate these voids from the velocity statistics. For the particles, the size of the remaining high-intensity clusters was used to distinguish between particles and background noise (bright clusters of flow tracers or particles located off of the measurement plane).

Compared to the single-phase (air only) data, the decoupled air phase results have a difference in the ensemble average and turbulent quantities magnitudes of less than 3% and 11% (for the baseline and forces cases, respectively) with very similar flow fields. These differences are assumed to be attributed to the particles' influence on the fluid-phase measurement. For example, Hassan et al. (1992), and Sakakibara et al. (1996) showed the fluid-phase, in the vicinity of large particles, was difficult to measure accurately using optical methods, such as PIV or PTV, due to the light scattering of the large particles (particle "halo" or "corona"). Also, particles located off of the measurement plane can be mistaken as fluid phase due to their lower light scattering, making the fluid-phase measurements less accurate. Thus, in many simultaneous measurement techniques, the fluid phase has shown a false influence by the particle due to fluid-phase measurement error. Therefore, it was decided to measure each phase separately.

3. Results and discussion

The interaction of an axisymmetric, particle-laden free jet with a single synthetic jet actuator (issued perpendicular to the main jet's streamwise axis) is presented in the following sections. First, the global effects of the synthetic jet at a fixed upstream distance on the three-dimensional time- and phase-averaged flow fields of the highest Stokes number particle-laden jet used is presented in Section 3.1. Section 3.2 presents the effects of the synthetic jet on three different Stokes number particle-laden jets. The weighted contribution of both the direct and indirect mechanisms of synthetic jet flow control is examined in Section 3.3. Note that the ef-

fect of the synthetic jet on a single-phase jet is discussed in greater detail in Tamburello and Amitay (2007b).

3.1. Three-dimensional flow field

In this section, the three-dimensional flow field resulting from the interaction of the *T*19 particle-laden free jet, which has the highest Stokes number tested, with and without the activation of a single synthetic jet is discussed. Because of its high Stokes number, the effect of flow control is expected to have the largest deviation from the effect on the single-phase flow field.

As described in Section 2, multiple two-dimensional *x*–*y* and *x*–*z* measurement planes were used to created three-dimensional renderings of the single-phase and *T*19 particulate phase flow fields. Fig. 2 presents three-dimensional renderings composed of three translucent iso-total-velocity surfaces ($V_{total}/U_e = V_{p,total}/U_e = 0.35$, 0.55, and 0.75) for the baseline (Fig. 2a and b) and time-averaged forced jets with $C_\mu = 0.005$ (Fig. 2c and d) and 0.16 (Fig. 2e and f) for the gas-phase (Fig. 2a, c and e) and *T*19 particulate phase (Fig. 2b, d and f). Note that a darker region exists in each of the *T*19 data within the potential core near the main jet exit due to the rendering software's attempt to add depth to the three-dimensional representations. These darker regions are equal to the highest contour values ($V_{p,total}/U_e = 0.75$). The total velocities for the carrier fluid (V_{total}/U_e) and particle-phase ($V_{p,total}/U_e$) are based on the streamwise, cross-stream, and spanwise velocity components (U, V, and W, and U_p, V_p, and W_p, respectively) as given by Eqs. (3.1) and (3.2):

$$\frac{V_{total}}{U_e} = \frac{\sqrt{U^2 + V^2 + W^2}}{U_e^2}, \tag{3.1}$$

$$\frac{V_{p,total}}{U_e} = \frac{\sqrt{U_p^2 + V_p^2 + W_p^2}}{U_e^2}. \tag{3.2}$$

For the carrier fluid, the baseline flow field (Fig. 2a) is axisymmetric about the jet's centerline. With a single synthetic jet activated at the lowest momentum coefficient used in this study ($C_\mu = 0.005$, Fig. 2c), the main jet flow field becomes asymmetric. As the momentum coefficient is increased ($C_\mu = 0.16$, Fig. 2e), the synthetic jet penetrates deeper into the main jet and spreading increases.

For the particulate phase, the baseline (Fig. 2b) is also axisymmetric about the main jet centerline. Note that the particle velocities are lower than the carrier fluid velocities near the main jet exit even though the highest contour levels have the same normalized total velocities. When the synthetic jet is activated, the iso-total-particle-velocity surfaces (Fig. 2d and f, $C_\mu = 0.005$ and 0.16, respectively) become asymmetric with increasing widths

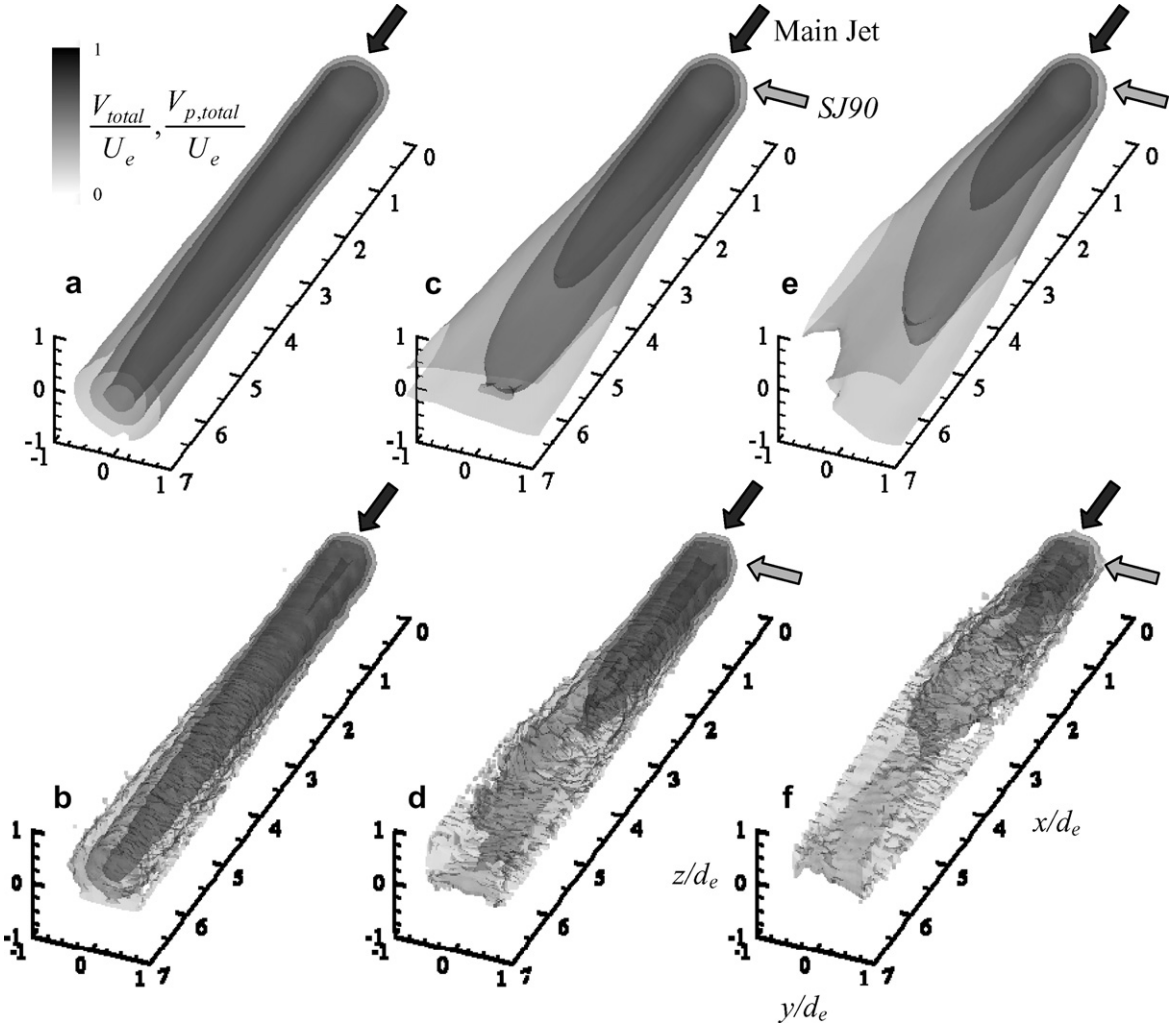

Fig. 2. Three-dimensional renderings of the single-phase iso-total velocity (a, c, e) and *T*19 particle iso-total velocity (b, d, f). Baseline (a, b) and forced jets with $C_\mu = 0.005$ (c, d) and 0.16 (e, f).

and decreasing velocity farther upstream as the momentum coefficient increases. These trends, which are less pronounced compared to the gas phase, can be explained through the synthetic jet's direct and indirect control mechanisms. Note that both of these control mechanisms change the drag force created by the carrier fluid acting on the particles. However, for the sake of discussion, these mechanisms will be described in terms of the fluid motion source rather than the resulting drag force. The synthetic jet impulse moves the particles *directly*, similar to the impulse of a continuous control jet. Conversely, the periodic motion of the synthetic jet amplifies the unstable modes of the carrier fluid creating large vortical structures that *indirectly* influence particle motion through preferential concentration (see Eaton and Fessler, 1994).

These two mechanisms can be better explained by examining the corresponding phase-averaged forced jets. Fig. 3 presents the three-dimensional iso-velocity renderings for the phase-averaged ($\phi = 180°$) gas (Fig. 3a and c) and particulate phases (Fig. 3b and d) at $C_\mu = 0.005$ (Fig. 3a and b) and 0.16 (Fig. 3c and d). At the lowest momentum coefficient, ($C_\mu = 0.005$, Fig. 3a), the synthetic jet yields an indentation in the gas phase jet's iso-surface on the side closer to the synthetic jet. Furthermore, large coherent structures (formed by the synthetic jet's actuation frequency) travel downstream as time progresses, resulting in a bending of the main jet flow (see Tamburello and Amitay, 2007b). As the momentum coefficient is increased ($C_\mu = 0.16$, Fig. 3c), the synthetic jet penetrates deeper into the gas phase jet as can be seen from the deeper indentation in the iso-surfaces.

For the particulate phase at $C_\mu = 0.005$ (Fig. 3b), the iso-total-particle-velocity rendering becomes *S*-shaped due to the indirect mechanism while maintaining velocities similar to the baseline (Fig. 2b) through $x/d_e \approx 4$. As the momentum coefficient is increased to $C_\mu = 0.16$ (Fig. 3d), the iso-surfaces become more distorted with decreased velocities farther upstream due to the increased direct effects (increased synthetic jet impulse). In addition, the phase-averaged iso-surfaces have indentations that result from the synthetic jet's impulse into the particle-laden jet, with larger indentations for increased momentum coefficients.

While the particle velocities are essential to understanding the particles' response to flow control, the velocity alone does not fully describe the relationship. The particle concentration, as given by the particle number density in Eq. (3.3), is also essential to understanding the particle's response to flow control.

$$\widehat{C}_{N_p} = \frac{C_{N_p}}{C_{N_{p,max}}} = \frac{N_p/A_{grid}}{N_{p,max}/A_{grid}} \tag{3.3}$$

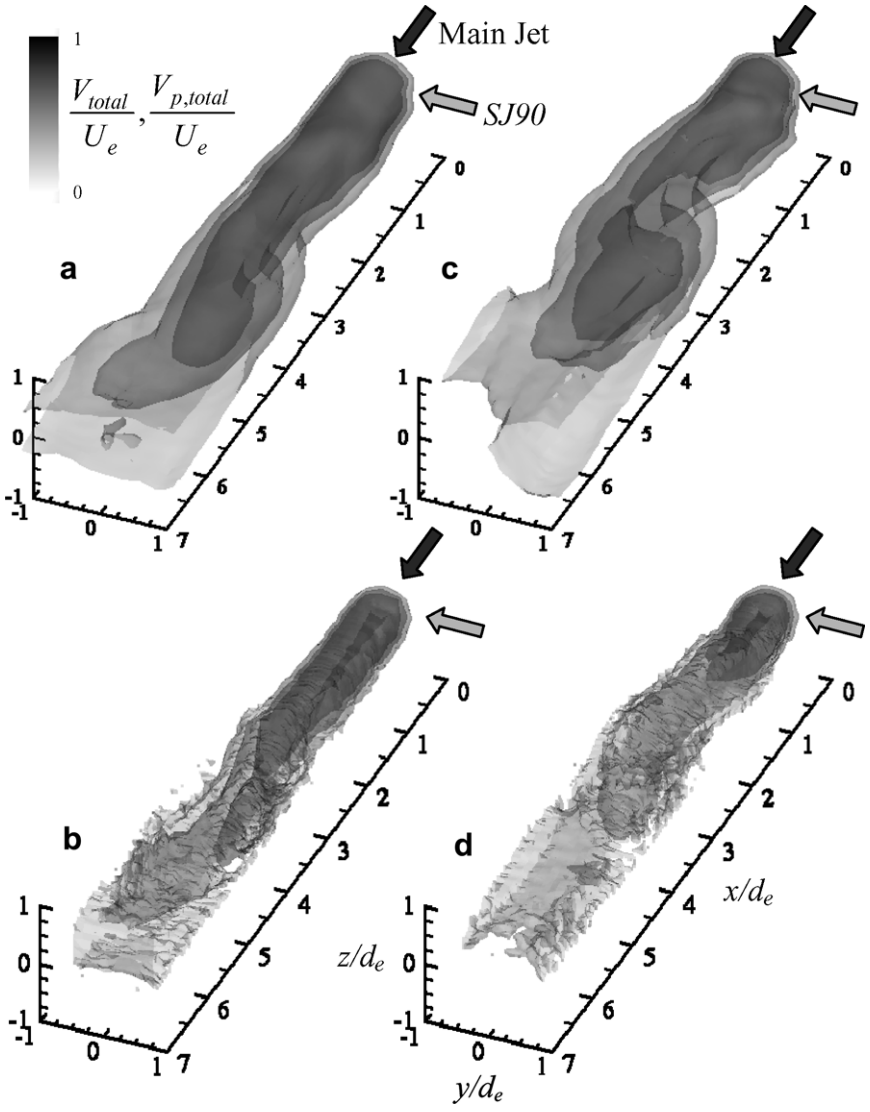

Fig. 3. Phase-averaged ($\phi = 180°$) maps of the single phase iso-total velocity (a, c) and *T*19 particle iso-total velocity (b, d). Forced jets with $C_\mu = 0.005$ (a, b) and 0.16 (c, d).

Here, N_p is the number of particles found at a given grid position, $N_{p,max}$ is the maximum number of particles within the measurement domain, A_{grid} is the area of a position on the measurement grid, C_{N_p} is the particle concentration at a given grid position, and $C_{N_{p,max}}$ is the maximum particle concentration within the measurement domain. Using the data reduction technique described in Section 2, the two-dimensional particle concentrations were transformed into three-dimensional particle renderings. Fig. 4 presents three-dimensional particle number density renderings composed of three translucent iso-$\widehat{C}_{N_p}$ surfaces ($\widehat{C}_{N_p} = 0.1$, 0.25, and 0.5) for the baseline (Fig. 4a), the time-averaged (Fig. 4b and d), and phase-averaged ($\phi = 180°$, Fig. 4c and e) jets with $C_\mu = 0.005$ (Fig. 4b and c) and 0.16 (Fig. 4d and e) for the *T*19 particle-laden jet.

The $\widehat{C}_{N_p}$ distribution for the baseline particle-laden jet (Fig. 4a) is axisymmetric about the jet centerline with highest concentrations along the centerline. When the synthetic jet is activated, the time-averaged $\widehat{C}_{N_p}$ distributions (Fig. 4b and d) have decreased magnitudes and increased spreading with increased effects for increasing momentum coefficient. The phase-averaged $\widehat{C}_{N_p}$ distributions (Fig. 4c and e) show the asymmetric, three-dimensional distortions seen in the total particle velocity renderings (Fig. 3b and d). At the lowest momentum coefficient ($C_\mu = 0.005$, Fig. 4c), the asymmetric distortions are relatively small and the $\widehat{C}_{N_p} = 0.25$ iso-surface extends to $x/d_e \approx 6$. As the momentum coefficient is increased ($C_\mu = 0.16$, Fig. 4e), the distortions become more pronounced throughout the measurement domain and the $\widehat{C}_{N_p}$ magnitude begins to decrease farther upstream.

As mentioned previously (see Section 2), the three-dimensional rendering technique used in this section does not have a high spatial resolution and, thus, shows only the global behavior. In order to better understand the small-scale structures and particle motions, the remainder of this work will present gas- and particulate-phase data in selected higher resolution two-dimensional measurement planes.

3.2. Stokes number effects

The effect of active flow control on different size particles (different *St*) was also investigated and is presented in this section. Note that each of the particle-laden jets had the same mass loading of $\gamma \approx 1\%$ and was forced with a single, perpendicular synthetic jet issued at $t_c/d_e = 0.4$.

Fig. 5 presents the normalized time-averaged streamwise velocity profiles along the *x*–*y* centerline plane of the baseline and forced jets with $C_\mu = 0.005$ and 0.16 at $x/d_e = 1$ (Fig. 5a, d, g and j), 3 (Fig. 5b, e, h and k), and 6 (Fig. 5c, f, i and l) for the single-phase (Fig. 5a–c) and the *T*01 (Fig. 5d–f), *T*09 (Fig. 5g–i), and *T*19

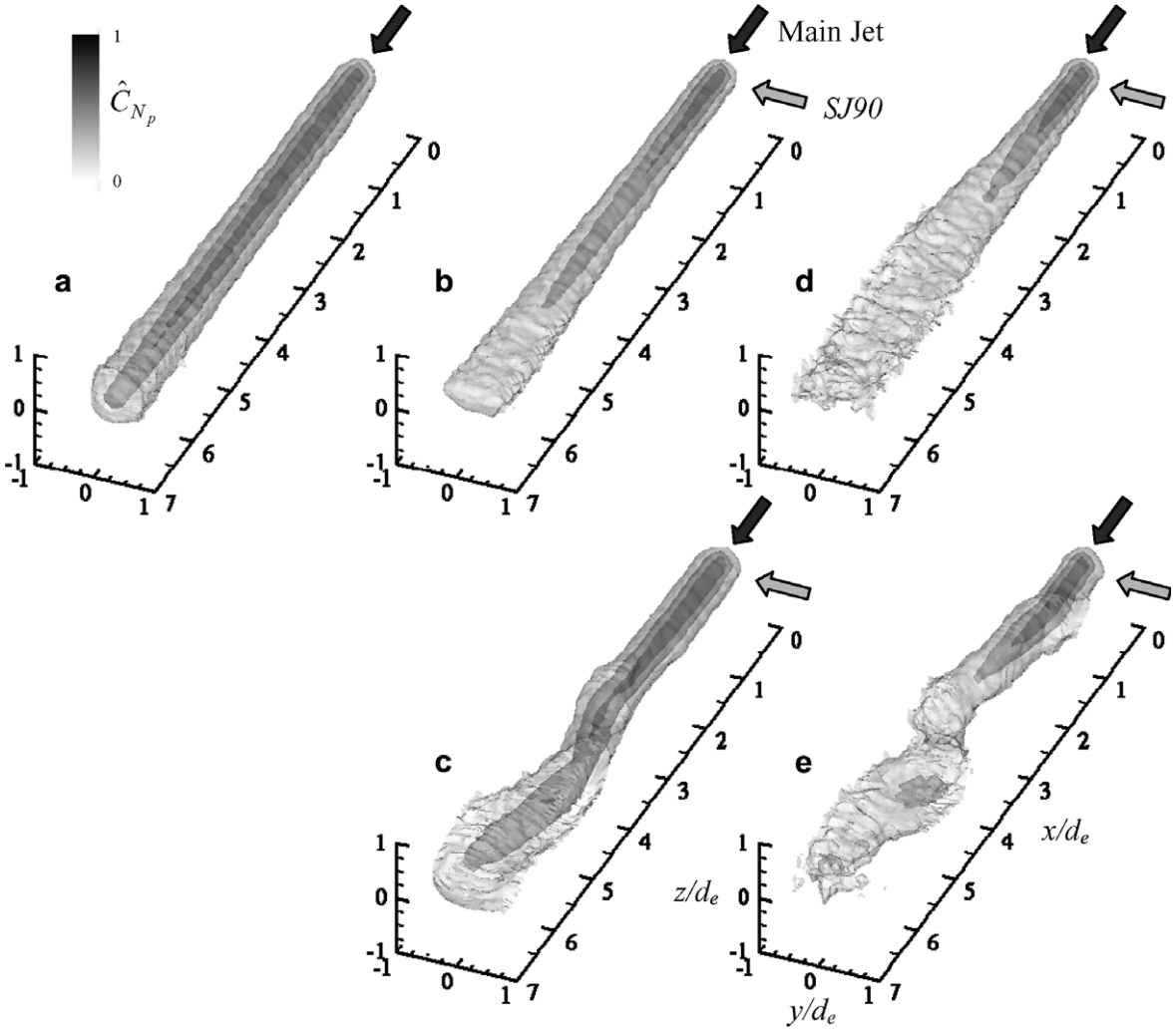

Fig. 4. Three-dimensional iso-particle number density maps of the *T*19 particles: time-averaged (a, b, d) and phase-averaged (c, e). Baseline (a) and forced jets with $C_\mu = 0.005$ (b, c) and 0.16 (d, e).

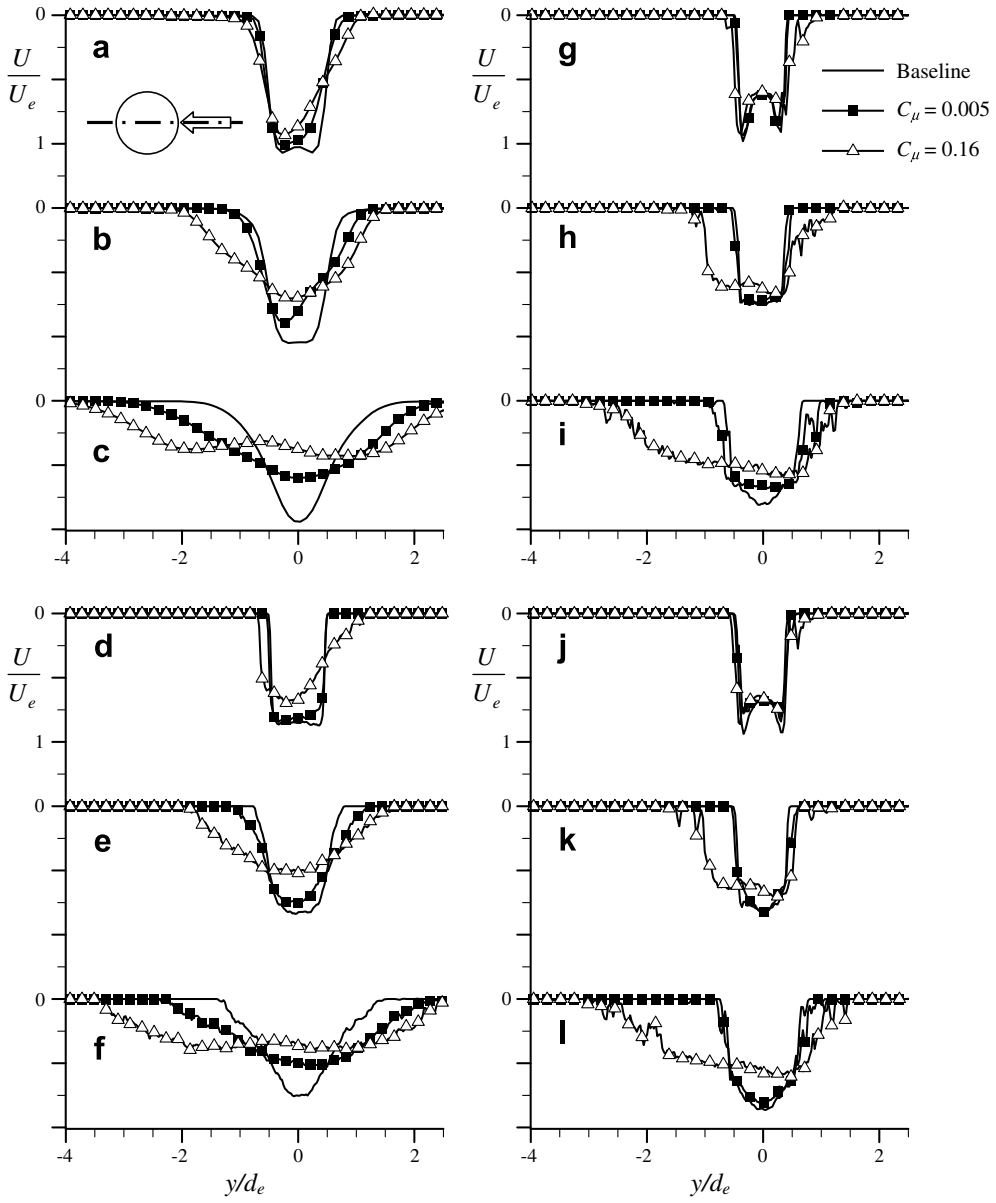

Fig. 5. Normalized time-averaged streamwise velocity profiles along the x–y centerline plane for the baseline and forced jet with $C_\mu = 0.005$ and 0.16 at $x/d_e = 1$ (a, d, g, j), 3 (b, e, h, k), and 6 (c, f, i, l) for the single-phase (a–c) and the *T*01 (d–f), *T*09(g–i), and *T*19 (j–l) particle-laden jets.

(Fig. 5j–l) particle-laden jets. The corresponding streamwise velocity profiles along the x–z centerline plane as well as the cross-stream and spanwise velocity profiles are presented in Figs. 6–8 respectively. Without flow control, the normalized streamwise velocity distributions (Fig. 5a–c and 6a–c, x–y and x–z planes, respectively) for the gas phase are symmetric about the x-axis, while the corresponding cross-stream (Fig. 7a–c) and spanwise (Fig. 8a–c) velocity profiles are anti-symmetric, as expected. In addition, the streamwise velocity profile near the main jet exit is uniform for ~80% of the orifice diameter, and its potential core extends to approximately $5d_e$.

With the synthetic jet activated at the lowest momentum ($C_\mu = 0.005$) for the single-phase jet (Fig. 5a–c), the cross-stream extent of the streamwise component (in the x–y plane) is increased in both directions and the peak magnitude is decreased for $x/d_e = 3$ and 6 (Fig. 5b and c, respectively). In addition, the main jet is vectored away from the synthetic jet side immediately downstream of the main jet exit and is tilted back toward the synthetic jet farther downstream. These trends may be attributed to the synthetic jet's impulse, which vectors the main jet away from the control side, as well as the growth of the vortical coherent structures due to the near-field periodic nature of the synthetic jet (within the range of unstable modes of the main jet), which vectors the main jet in both directions.

As the momentum coefficient is increased ($C_\mu = 0.16$), the jet is wider (than the $C_\mu = 0.005$ case) and is vectored both away from and toward the synthetic jet, where the cross-stream distribution of velocity exhibits a double peak distribution for $x/d_e > 3.5$. These trends further support the speculation of the two mechanisms associated with the interaction of the synthetic jet with the main jet.

It has been established in the literature (Saffman, 1962; Hetsroni, 1989; Eaton and Fessler, 1994; and others) that low Stokes number flows are more responsive to the carrier fluid and, thus, follow its downstream distribution more closely, as shown for the *T*01 particle-laden jet (Fig. 5d–f). The baseline streamwise velocity profiles have a relatively uniform (top-hat velocity) cross-section at $x/d_e = 1$ (Fig. 5d), which corresponds to the region

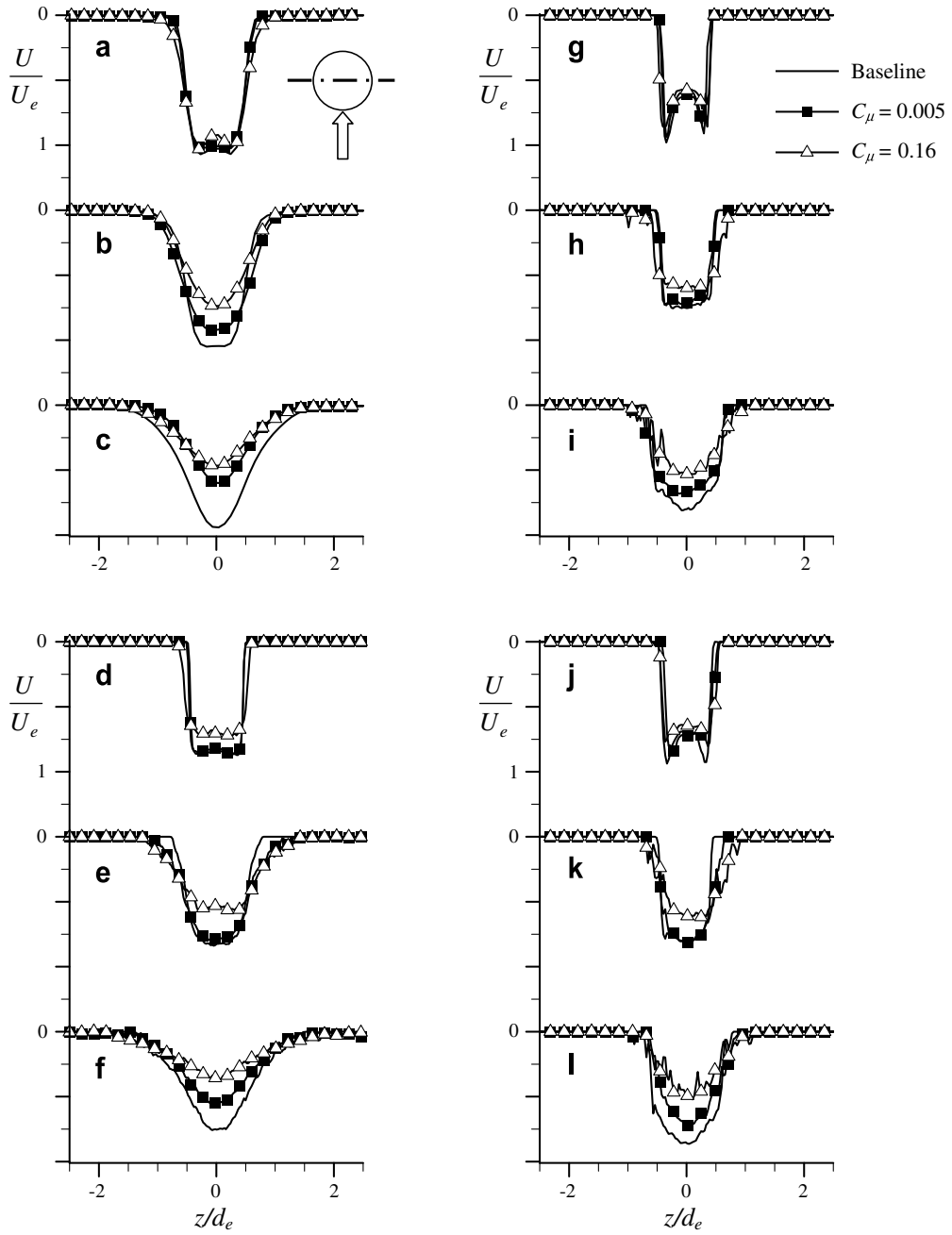

Fig. 6. Normalized time-averaged streamwise velocity profiles along the x–z centerline plane for the baseline and forced jet with $C_\mu = 0.005$ and 0.16 at $x/d_e = 1$ (a, d, g, j), 3 (b, e, h, k), and 6 (c, f, i, l) for the single-phase (a–c) and the *T*01 (d–f), *T*09(g–i), and *T*19 (j–l) particle-laden jets.

of constant width potential core for the gas-phase jet. Farther downstream (Fig 5e and f), particle dispersion takes place in the shear layers due to the fluid circulation of the vortex rings, which are formed in the instantaneous carrier fluid (not shown). This results in ejection of the particles outward from the centerline. In addition, the velocity profiles become more rounded, similar to those seen for the gas phase.

With the synthetic jet activated, the *T*01particles (Fig 5d–f) are vectored both toward and away from the synthetic jet side, with increased vectoring for increased momentum coefficients. These trends can be attributed to both the *direct* impulse of the synthetic jet as well as the amplification of the carrier fluid's coherent vortical structures, resulting in larger velocity magnitudes. In addition, the *T*01particles have similar streamwise velocity profiles, in both magnitude and distribution width, to those of the gas phase jets, which suggests that the low Stokes number particles follow the carrier fluid. Note that the high momentum coefficient *T*01particle case has a double-peak distribution for $x/d_e = 6$ (Fig. 5f), similar to the single-phase forced jet (Fig. 5c).

For the larger Stokes number particles (*T*09 and *T*19 particles, Fig. 5g–i and j–l, respectively), the baseline particle-laden jets are very similar to one another. Each has double-peak distribution near the main jet exit (*T*09 and *T19*, Fig. 5g and j, respectively), where the minimum velocity between the peaks corresponds to the region of highest particle concentration (as will be shown in Fig. 9). At $x/d_e = 3$, as the particles are advected off of the jet centerline, the velocity profiles become relatively uniform (Fig. 5h and k, *T*09 and *T*19, respectively), becoming more rounded farther downstream (Fig. 5i and l, *T*09 and *T*19, respectively).

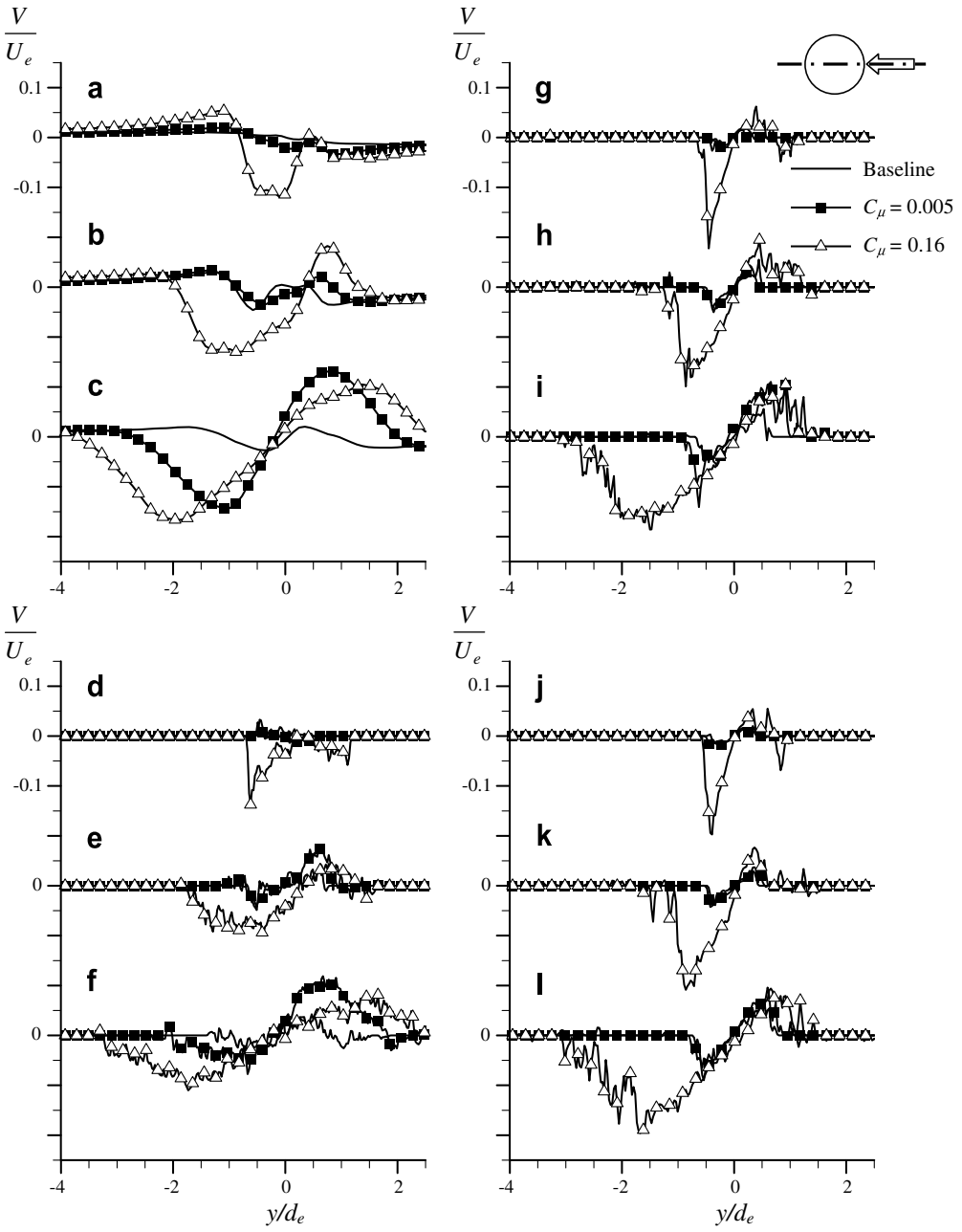

Fig. 7. Normalized time-averaged cross-stream velocity profiles along the x–y centerline plane for the baseline and forced jet with $C_\mu = 0.005$ and 0.16 at $x/d_e = 1$ (a, d, g, j), 3 (b, e, h, k), and 6 (c, f, i, l) for the single-phase (a–c) and the *T01* (d–f), *T*09(g–i), and *T*19 (j–l) particle-laden jets.

With the synthetic jet activated, the larger Stokes number particles (*T*09 and *T*19 particles, Fig. 5g–i and j–l, respectively) do not follow the carrier fluid as closely as the *T*01particles do. For $C_\mu = 0.005$, the synthetic jet increases particle spreading both toward and away from the control side, but to a much lesser extent than the *T*01particles. As the momentum coefficient is increased, the particle-laden jet width is further increased and more of the particles are vectored away from the synthetic jet side. This might be attributed to the direct effect, which is more pronounced for the larger Stokes number.

Similar results are shown along the x–z centerline plane (Fig. 6), where the synthetic jet slightly widens the velocity fields (compared to the baselines) throughout the measurement plane for the gas- and *T*01, *T*09, and *T*19 cases (Fig. 6a–i and j–l, respectively). The velocity magnitudes decrease with increasing momentum coefficient as the forced single-phase and particle-laden jets are vectored out of the measurement plane. As for the x–y centerline plane, the velocity field of the lower Stokes number (*T*01) particle-laden jet in the x–z centerline plane is similar to the single-phase jet with larger spreading than the higher Stokes number (*T*09 and *T*19) particle-laden forced jets.

The synthetic jet also causes a significant increase in the cross-stream velocity on both sides of the single-phase jet (Fig. 7a–c), as well as the *T*01 (Fig. 7d–f), *T*09 (Fig. 7g–i), and *T*19 (Fig. 7j–l) particle-laden jets in the x–y centerline plane, especially farther downstream (at $x/d_e = 3$ and 6). This trend is indicative of increased spreading in the x–y direction. By contrast, the spanwise velocity along the x–z centerline plane (Fig. 8) is also increased by the synthetic jet, but to a much lesser extent than in the cross-stream

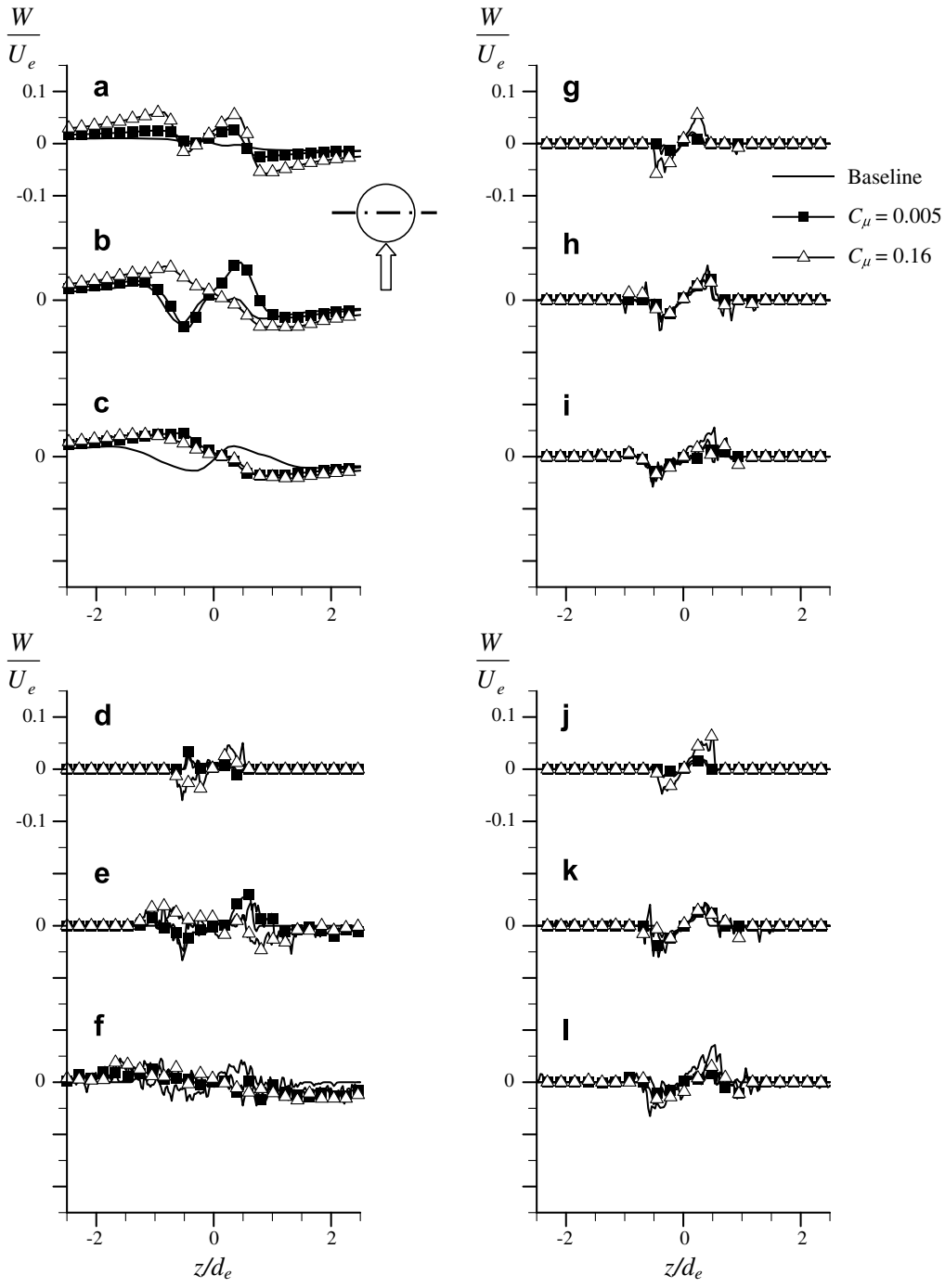

Fig. 8. Normalized time-averaged spanwise velocity profiles along the x–z centerline plane for the baseline and forced jet with $C_\mu = 0.005$ and 0.16 at $x/d_e = 1$ (a, d, g, j), 3 (b, e, h, k), and 6 (c, f, i, l) for the single-phase (a–c) and the *T*01 (d–f), *T*09(g–i), and *T*19 (j–l) particle-laden jets.

direction. This can be attributed to the carrier fluid and particles being vectored out of measurement plane.

Next, the particle distributions, as depicted in the particle number densities in Figs. 9 and 10 (in the x–y and x–z centerline planes, respectively) were examined to better understand the effect of synthetic jet flow control. Fig. 9 presents the time-averaged vorticity distributions of the carrier fluid (Fig. 9a, e and j) and normalized particle number density distributions (Fig. 9b, f and j; c, g and k; and d, h and l; *T*01, *T*09 and *T*19, respectively) for the baseline (Fig. 9a–d) and forced jets with $C_\mu = 0.005$ (Fig. 9e–h) and 0.16 (Fig. 9i–l) in the x–y centerline plane, with the corresponding distributions along the x–z centerline plane in Fig. 10.

The baseline gas-phase jet's normalized spanwise vorticity distribution ($\hat{\Omega}_z$, Fig. 9a) is antisymmetric about the x-axis, with positive vorticity along the left-side shear layer and negative vorticity (marked by dashed lines) along the right-side shear layer, as expected. When the synthetic jet is activated (Fig. 9e and i, $C_\mu = 0.005$ and 0.16, respectively), the vorticity distributions are extended both toward and away from the synthetic jet for both momentum coefficients, with decreasing magnitudes farther upstream (compared to the baseline) with increasing momentum coefficient. At the highest momentum coefficient ($C_\mu = 0.16$, Fig. 9i), a secondary negative-vorticity region forms within the positive vorticity region for $x/d_e > 4.2$ marking the

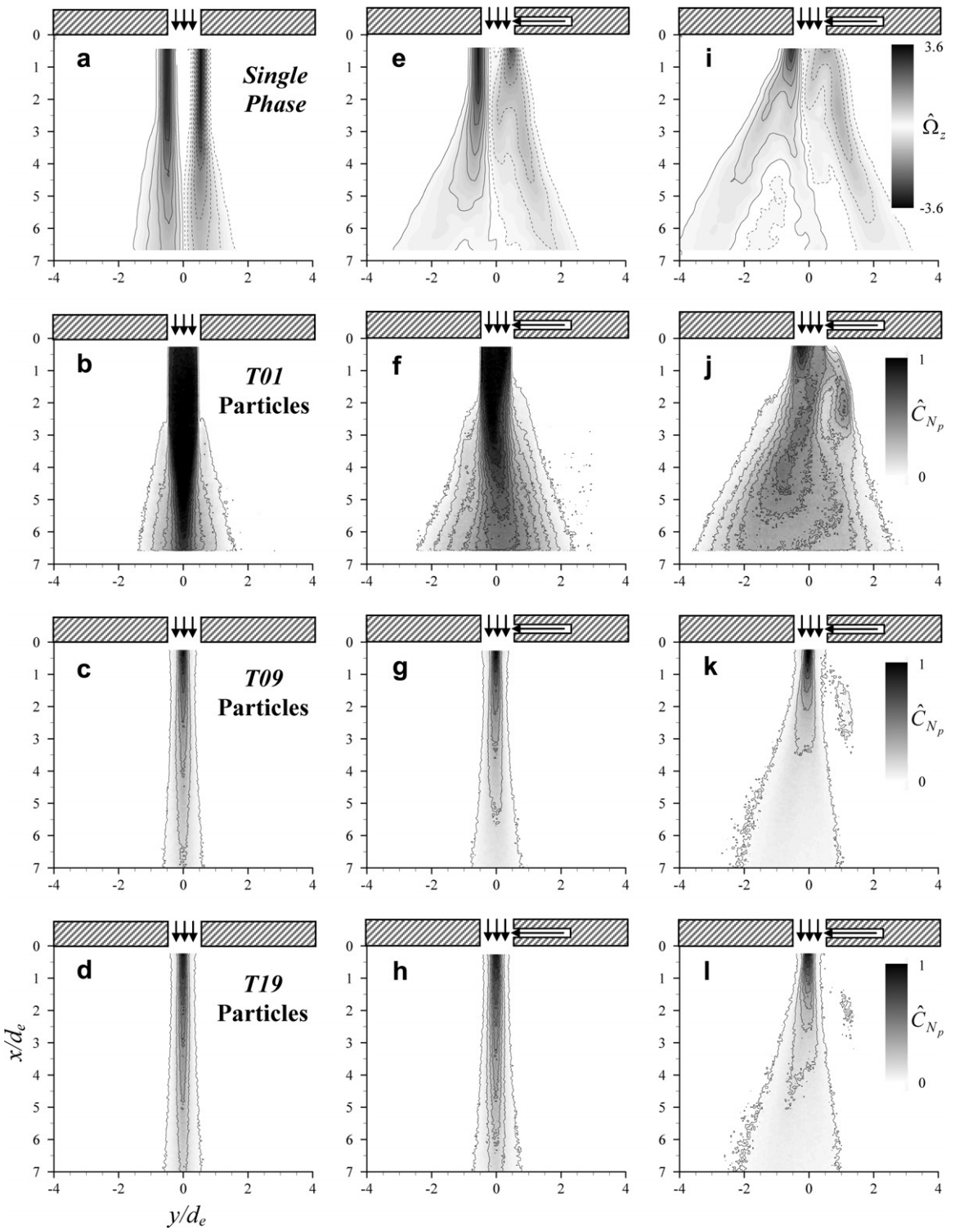

Fig. 9. Normalized spanwise vorticity (a, e, i) and particle number density (b–d, f–h, j–l) contours for the baseline (a–d) and forced jets with C_μ = 0.005 (e–h) and 0.16 (i–l) for the single-phase (a, e, i) and the *T*01(b, f, j), *T*09(c, g, k), and *T19* (d, h, l) particles in the *x*–*y* centerline plane.

valley in the double-peak distribution seen in the velocity vector field (Fig. 5c).

For the baseline *T*01 jet (Fig. 9b), the $\widehat{C}_{N_p}$ distribution has a relatively uniform cross-section for $x/d_e < 2$, which corresponds to the region of the constant-width potential core for the gas-phase jet (Fig. 9a). Farther downstream, particle dispersion takes place in the shear layers due to the vortex rings, which are formed in the instantaneous carrier fluid, that eject the particles outward from the centerline. Note that the highest particle concentrations are within the main jet potential core where the cross-stream velocity of the carrier fluid is minimal.

For the baseline *T*09 and *T*19 jets (Fig. 9c and d, respectively), the highest particle concentrations are along the *x*-axis, but the concentration drops significantly with downstream distance as the particles spread off of the main jet centerline. However, unlike the smaller *T*01 particles, the *T*09 and *T19* particles remain

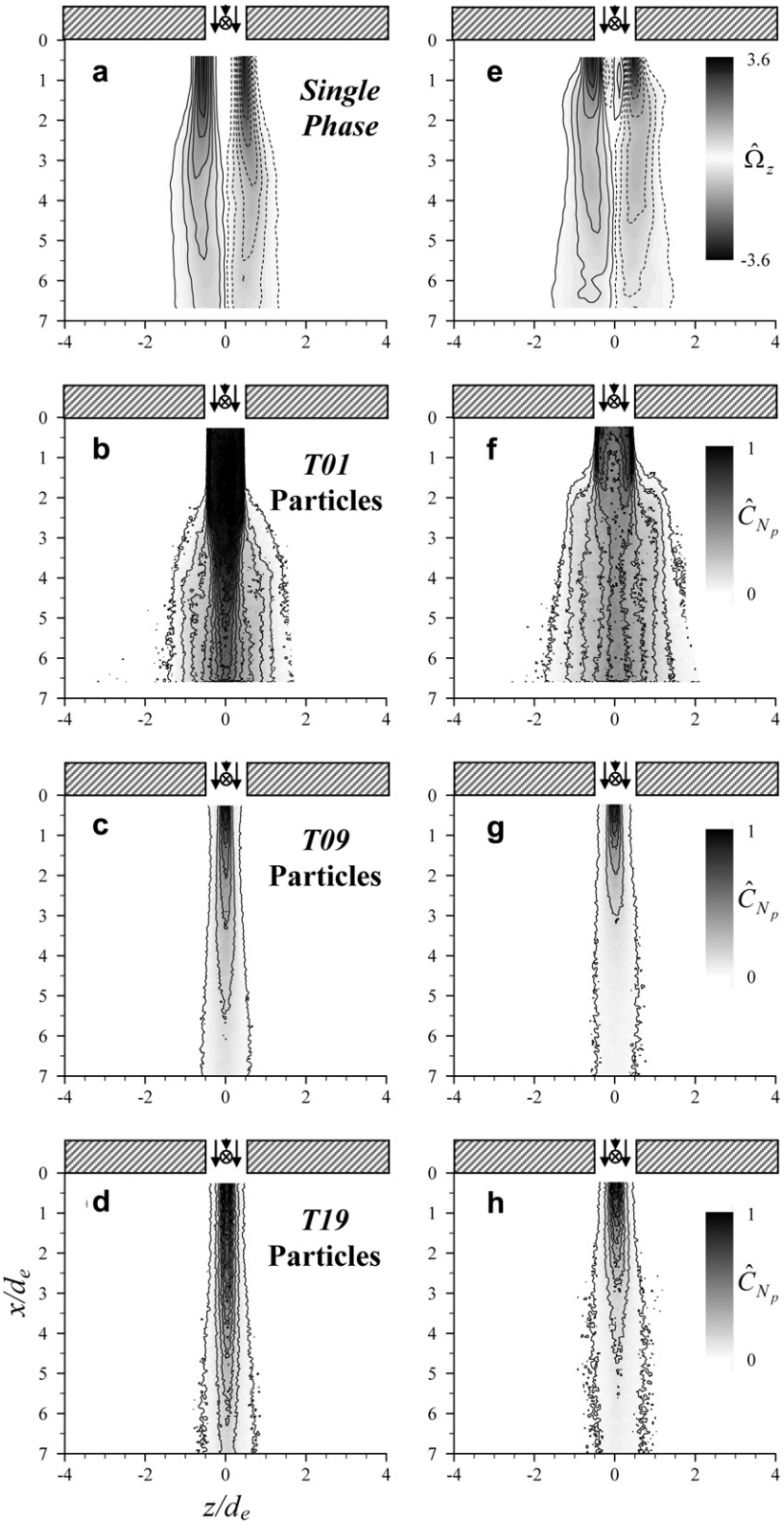

Fig. 10. Normalized spanwise vorticity (a, e) and particle number density (b–d, f–h) contours for the forced jets with C_μ = 0.005 (a–d) and 0.16 (e–h) for the single-phase (a, e) and the *T*01(b, f), *T*09(c, g), and *T*19 (d, h) particles in the *x*–*z* centerline plane.

in a narrow column along the centerline. The regions of highest particle concentration correspond to the minimum particle velocities between the peaks in the corresponding velocity fields (Fig. 5g–i and j–l). In addition, the cross-stream extent of the *T*19 particle concentration fields is slightly narrower than the *T*09 particles.

When the synthetic jet is activated, the $\widehat{C}_{N_p}$ distributions of the smallest particles tested (*T*01, Fig. 9f and j) along the *x*–*y* centerline

plane are much wider, where the highest magnitudes extend for $x/d_e < 3.5$ and 0.9 ($C_\mu = 0.005$ and 0.16, respectively). As the momentum coefficient increases, the spreading begins farther upstream. In addition, the *T01* particle distributions have widths that resemble the gaseous phase vorticity distributions (Fig. 9e and j), which is indicative of the *T*01 particles following the gas-phase well.

For the higher Stokes number particles (*T*09 and *T*19 particles, Fig. 9g and k and 9h and l, respectively), the particles are mainly spread away from the synthetic jet side (due to the direct effect) and the particle concentration decreases farther upstream, with the effects increasing with increased momentum coefficient. Note that, for $C_\mu = 0.16$ (Fig 9k and l, *T*09 and *T*19 particles, respectively), there is a concentration of particles outside of the main jet flow for $1 < x/d_e < 3$, $0.6 < y/d_e < 1.3$, which correspond to particles that have been thrown away from the main jet by large vortical structures. This will be discussed in more detail below. Comparing the *T*09 and *T*19 particles, the $\widehat{C}_{N_p}$ distributions are quite similar even though the Stokes number is doubled, which may imply that there is a range of Stokes numbers much greater than unity that has similar responses to the carrier fluid.

Similar results are shown along the *x*–*z* centerline plane (Fig. 10), where the synthetic jet slightly widens the $\widehat{C}_{N_p}$ distributions (compared to the baselines) throughout the measurement plane for each of the particle classes. The $\widehat{C}_{N_p}$ magnitudes decrease with increasing momentum coefficient as the particles are vectored out of the measurement plane. As for the *x*–*y* centerline plane, the lower Stokes number (*T*01) particle-laden forced jet in the *x*–*z* centerline plane has similar $\widehat{C}_{N_p}$ distributions to the to single-phase vorticity distributions, with larger distribution widths than the higher Stokes number (*T*09 and *T*19) particle-laden forced jets.

Next, the effect of the synthetic jet on the particulate and carrier fluid velocity fluctuations was investigated by calculating the planar RMS velocity according to Eqs. (3.4) and (3.5) for the gas and particle velocities, respectively.

$$\frac{V_{\mathrm{RMS,planar}}}{U_e} = \frac{\sqrt{U_{\mathrm{RMS}}^2 + V_{\mathrm{RMS}}^2}}{U_e} \tag{3.4}$$

$$\frac{V_{\mathrm{p,RMS,planar}}}{U_e} = \frac{\sqrt{U_{\mathrm{p,RMS}}^2 + V_{\mathrm{p,RMS}}^2}}{U_e} \tag{3.5}$$

Here, U_{RMS} and V_{RMS} are the streamwise and cross-stream RMS velocities, respectively, for the gas phase, and $U_{\mathrm{p,RMS}}$ and $V_{\mathrm{p,RMS}}$ are the streamwise and cross-stream particle RMS velocities, respectively.

Fig. 11 presents the normalized planar RMS velocity distributions for the gas (Fig. 11a, e and i) and particle (Fig. 11b, f and j; c, g and k; and d, h and l; *T*01, *T*09, and *T*19, respectively) phases for the baseline (Fig. 11a–d) and forced jets with $C_\mu = 0.005$ (Fig. 11e–h) and 0.16 (Fig. 11i–l) along the *x*–*y* centerline plane, with the corresponding planar RMS velocity distributions along the *x*–*z* centerline plane in Fig. 12. Note that the contour lines correspond to $V_{\mathrm{RMS,planar}}/U_e = V_{\mathrm{p,RMS,planar}}/U_e = 0.1, 0.3, 0.5, 0.7, 0.8, 0.9$, and 1.0.

For the single-phase jet (Fig. 11a), the planar RMS velocity is symmetric about the *x*-axis with its largest magnitudes in the potential core closest to the main jet exit on both sides of the jet and decreasing magnitude with radial distance from the jet centerline and downstream distance ($x/d_e > 2$). When the synthetic jet is activated, the RMS velocity (Fig. 9e and i, $C_\mu = 0.005$ and 0.16, respectively) shows decreased magnitudes and increased width with downstream distance. As the momentum coefficient increases, the RMS levels throughout the flow field decrease. Note the double-peak concentrations for $x/d_e > 4$, corresponding to the double-peak distribution in the velocity field.

Similar to the single-phase jet, the baseline *T*01 particle-laden jet (Fig. 11b) has a symmetric RMS velocity distribution with its highest values within the potential core. However, the highest magnitudes are located along the shear layers of the potential core for $x/d_e < 2.5$, which corresponds to the regions of highest velocity gradient for the carrier fluid. The *T*09 and *T*19 particles (Fig. 11c and d, respectively) have similar double-peak planar particle RMS velocity distributions with regions of highest magnitude along the shear layer near the main jet exit ($x/d_e < 1.5$), which correspond to the peak velocities at these locations (as seen in Fig. 5g–i and j–l, respectively). Farther downstream ($x/d_e > 2.5$), the particle-laden jets have single-peak distributions with their highest values along the main jet centerline.

When the synthetic jet is activated ($C_\mu = 0.005$ and 0.16, Fig. 11f and j, respectively), the planar particle RMS velocity distributions for the *T*01 particles are similar to the corresponding single-phase flow distributions (Fig. 11e and i, respectively), but with lower magnitudes and slightly narrower distribution widths. As the momentum coefficient is increased, the magnitude decreases and the distribution width increases farther upstream.

For the higher Stokes number particles ($C_\mu = 0.005$, *T09* and *T*19, Fig. 11g and h, respectively), the planar particle RMS distributions are similar to the baselines (Fig. 11c and d, respectively) for $x/d_e < 3$, with double-peak distributions that have their highest magnitudes along the shear layer. Farther downstream ($x/d_e > 3$), the magnitude decreases and the profiles exhibit single-peak distributions while their cross-stream extent is larger (compared to the baselines). As the momentum coefficient is increased ($C_\mu = 0.16$, Fig. 11h and l), the RMS distribution remains double-peaked near the main jet exit ($x/d_e < 1.5$) while, farther downstream, the distribution width is further increased and the magnitudes are further decreased. There are additional regions of velocity fluctuations along the side closer to the synthetic jet ($0.7 < y/d_e < 2$) that correspond to particles drawn out of the main jet flow by large vortical structures of the carrier fluid (discussed later).

Similar trends are shown for the normalized planar RMS velocity distributions in the plane perpendicular to the synthetic jet (*x*–*z* centerline plane, Fig. 12). The normalized planar RMS velocity distributions are symmetric about the *x*-axis for both the single-phase and particle-laden (all three particle classes) forced jets, with decreasing magnitude farther downstream as the momentum coefficient is increased.

In order to further understand the evolution and dispersion of the forced particle-laden jets, phase-averaged data for each particle size were acquired and are presented in Figs. 13–15. Figs. 13 and 14 present the particle number density (line format) superimposed onto the single-phase vorticity distributions (flood format) along the *x*–*y* and *x*–*z* centerline planes, respectively. To highlight the relationship between the coherent structures in the carrier fluid and the particulate phase, Fig. 15 presents the particle velocity vectors superimposed onto the vorticity field for the dashed regions in Fig. 13. Note that the $\widehat{C}_{N_p}$ contour lines correspond to 0.01, 0.1, 0.2, 0.3, . . . , 1.0. In addition, note that the vorticity distributions do not provide differentiation between negative and positive vorticity because they are used to present the location of the vortical structures.

Fig. 13 presents the phase-averaged flow fields ($\phi = 180°$) with $C_\mu = 0.005$ (Fig. 13a–c) and 0.16 (Fig. 13d–f) for the *T*01 (Fig. 13a and d), *T*09 (Fig. 13b and e), and *T*19 (Fig. 13c and f) particle-laden jets in the *x*–*y* centerline plane, while the corresponding *x*–*z* centerline planes are shown in Fig. 14. According to preferential concentration (Eaton and Fessler, 1994), particles can be *indirectly* affected by vortical structures, present in the carrier fluid, by causing the particle to accumulate in highly strained regions between vortical structures as the particles are unable to penetrate the cores

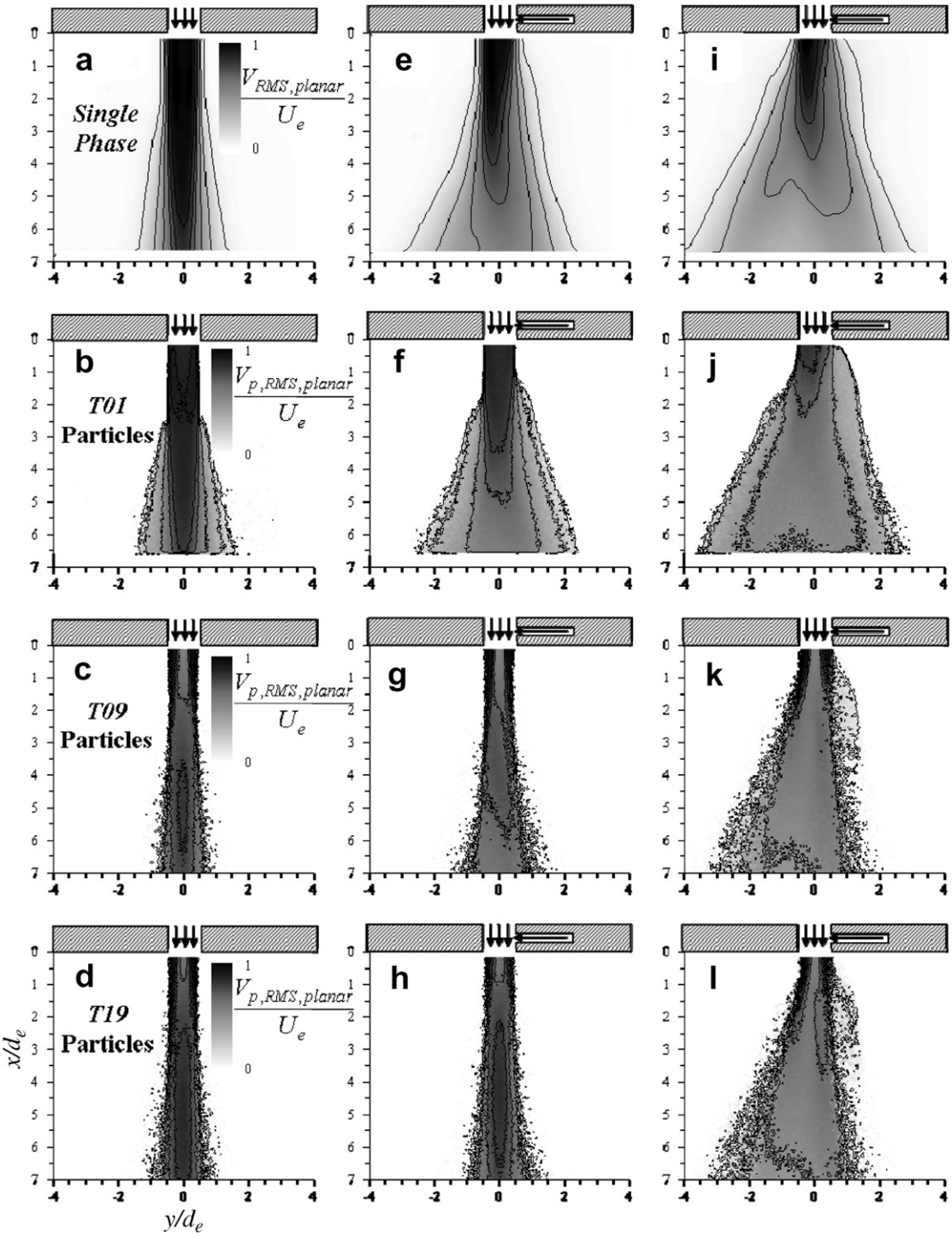

Fig. 11. Normalized planar RMS velocity fields for the baseline (a–d) and forced jets with C_μ = 0.005 (e–h) and 0.16 (i–l) for the single-phase (a, e, i) and the *T*01(b, f, j), *T*09(c, g, k), and *T*19 (d, h, l) particles in the *x*–*y* centerline plane.

of the vortical structures. In addition, the impulse of the synthetic jet also *directly* moves the particles away from the control.

When the synthetic jet is activated at C_μ = 0.005 (Fig 13a, b, and c; *T*01, *T*09, and *T*19 particles, respectively), the *direct* effects of the synthetic jet impulse are small compared to the *indirect* effects. The *T*01 particles (Fig. 13a), which have the lowest Stokes number ($St^*_{f,25m/s} = 0.703$), are the most responsive to the carrier fluid motions. Conversely, the *T*09 and *T*19 particles (Fig. 11b and c, respectively), which have Stokes numbers that are an order of magnitude larger ($St^*_{f,25m/s} = 4.72$ and 9.31, respectively), are less responsive to the carrier fluid motions and mainly remain along the centerline throughout the measurement planes with only small deviations from the centerline toward the end of the measurement domain. These deviations can be attributed to the large vortical structures, resulting from the change in fluid velocity, seen by the particles that drag the particles off of the centerline.

At the highest momentum coefficient (C_μ = 0.16, Fig. 13d, e, and f; *T*01, *T*09, and *T*19 particles, respectively), both the *direct* and *indirect* mechanisms are much larger because the synthetic jet is much stronger (higher momentum coefficient), resulting in stronger

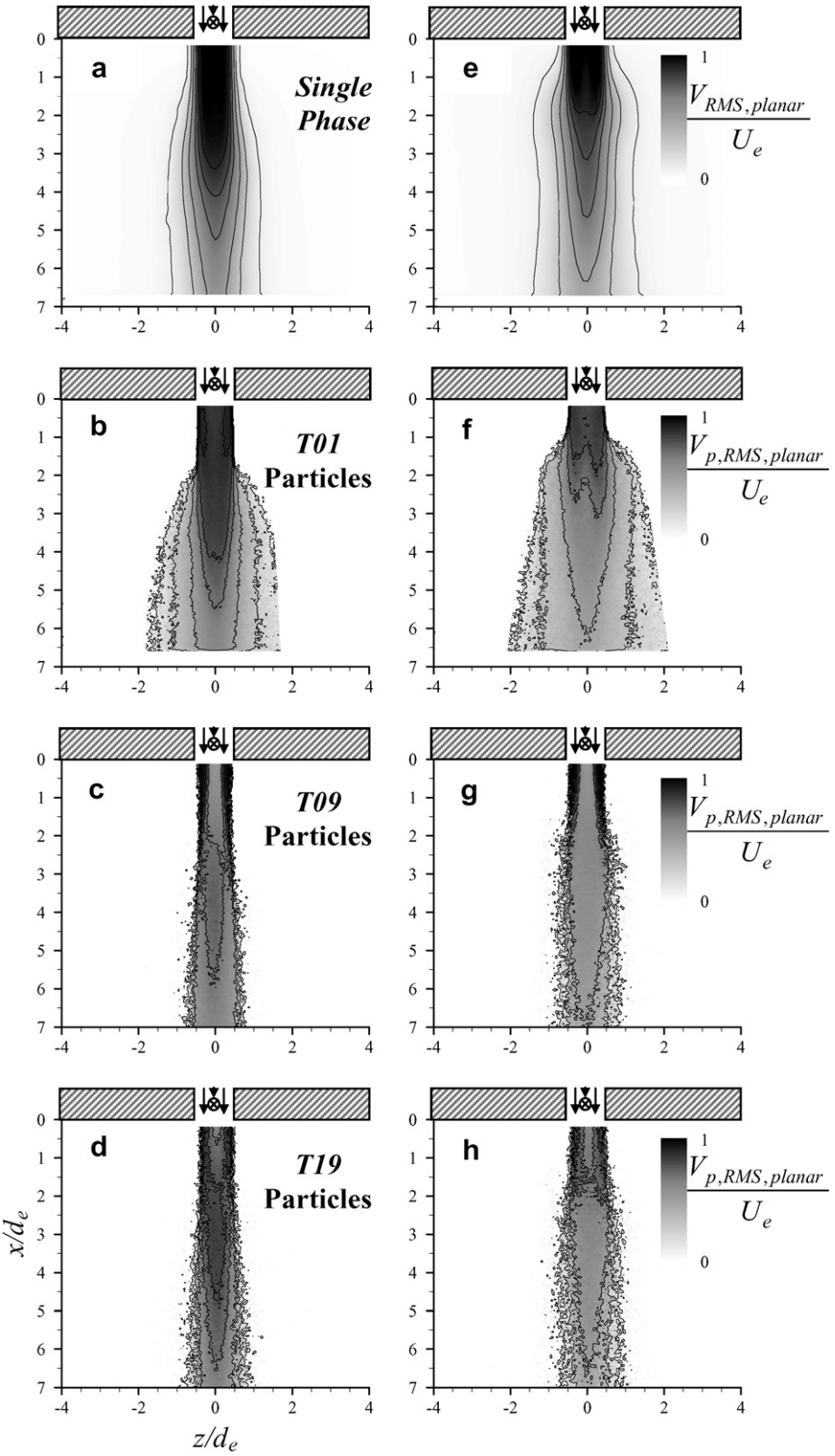

Fig. 12. Normalized planar RMS velocity fields for the forced jets with $C_\mu = 0.005$ (a–d) and 0.16 (e–h) for the single-phase (a, e) and the *T*01(b, f), *T*09(c, g), and *T*19 (d, h) particles in the *x*–*z* centerline plane.

coherent structures (~80% increase in circulation) as well as increased impulses such that the particles deviate from the main jet centerline to a greater extent with increased spreading in the spanwise direction. The particles cluster just downstream of the vortical structures (in the highly strained regions) and are pulled from the clusters by the outward-moving flow along the downstream edge of the vortical structures according to preferential concentration (Eaton and Fessler, 1994). This is especially promi-

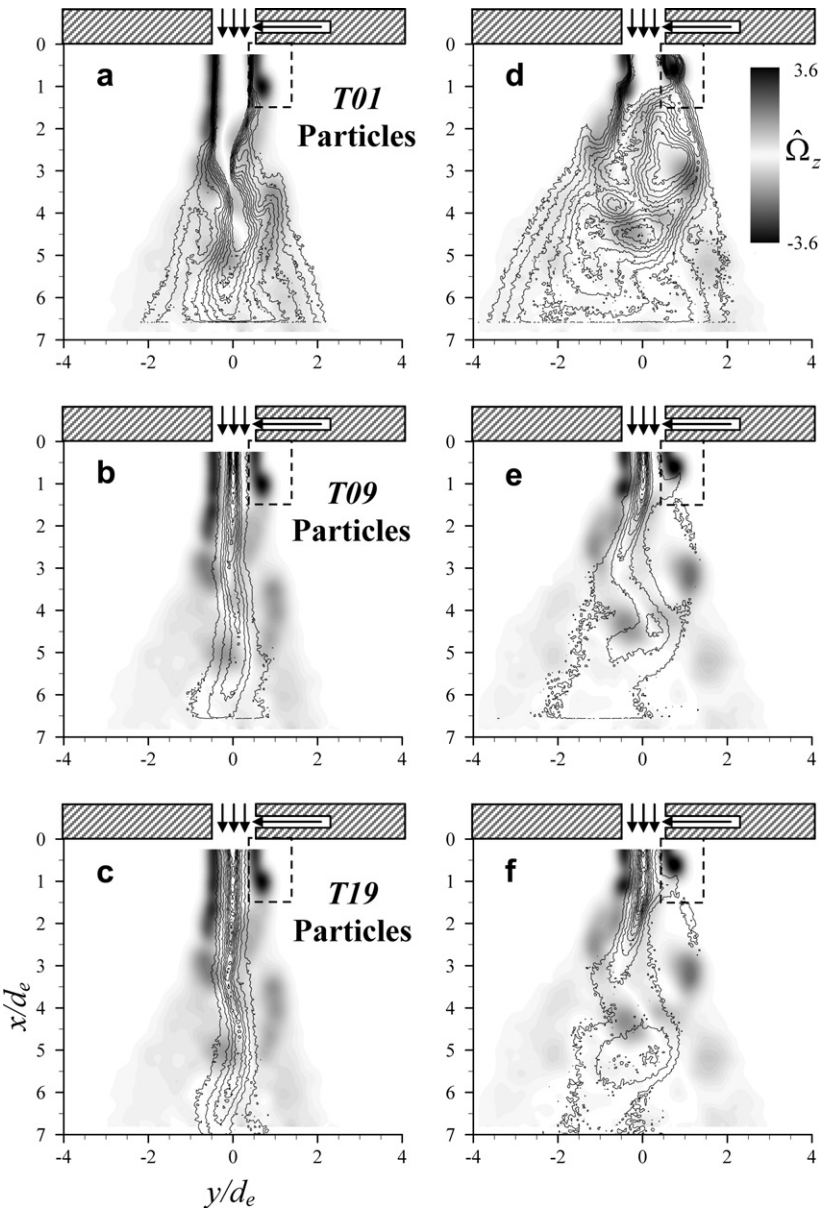

Fig. 13. Phase-averaged ($\phi = 180°$) normalized particle number density distributions (lines) superimposed on the corresponding single-phase vorticity fields (floods) with $C_\mu = 0.005$ (a–c) and 0.16 (d–f) for the *T*01(a, d), *T*09(b, e), and *T*19 (c, f) particles in the *x*–*y* centerline plane.

nent for the *T*01 particles (Fig. 13d) where the $\widehat{C}_{N_p}$ distribution extends to the edges of the carrier fluid vorticity distributions. While the *T*09 and *T*19 particles (Fig. 13e and f, respectively) also show larger distortions of the $\widehat{C}_{N_p}$ distributions (than the $C_\mu = 0.005$ cases), they deviate from the centerline to a lesser extent than the *T*01 particles and do not follow the large vortical structures as the smaller particles do. Note that the vortical structures induce lateral drag force (via changes in the velocity field) on the particles, which drags them away from the main jet centerline. The higher the maximum vorticity magnitude, the larger the velocity and resulting lateral drag force and, thus, the more particles are affected by the vortical structures. In addition, the lower the particle Stokes number, the more effective the vortical structures are at dragging the particles.

Similar results are shown in the *x*–*z* centerline plane (Fig. 14), where the distributions remain symmetric with particles clustered upstream and downstream of the large vortical structures and more particles being drawn and/or forced away from the centerline for increased synthetic jet momentum coefficients and smaller particle Stokes numbers.

The above trends show that each of the particle cases is influenced *directly* by the synthetic jet's impulse as well as *indirectly* by the resulting coherent vortical structures. The *T*01 particles are the most responsive to changes in the carrier fluid and follow the fluid flow fairly closely. By contrast, the *T*09 and *T*19 particles, which have Stokes numbers that are an order of magnitude larger than the *T*01 particles, are much less responsive to the carrier fluid and do not follow the bulk of the fluid flow except for the stronger vortical structures (higher circulation). In addition, the *T*09 and *T*19 particles have fairly similar responses to the forced flow, with the *T*09 particles being slightly more responsive due to their lower Stokes number.

While the position of the particles with respect to the vortical structures, as given by the particle number density, is essential to understanding the particle's response to flow control, the position alone does not fully describe the relationship. Thus, Fig. 15

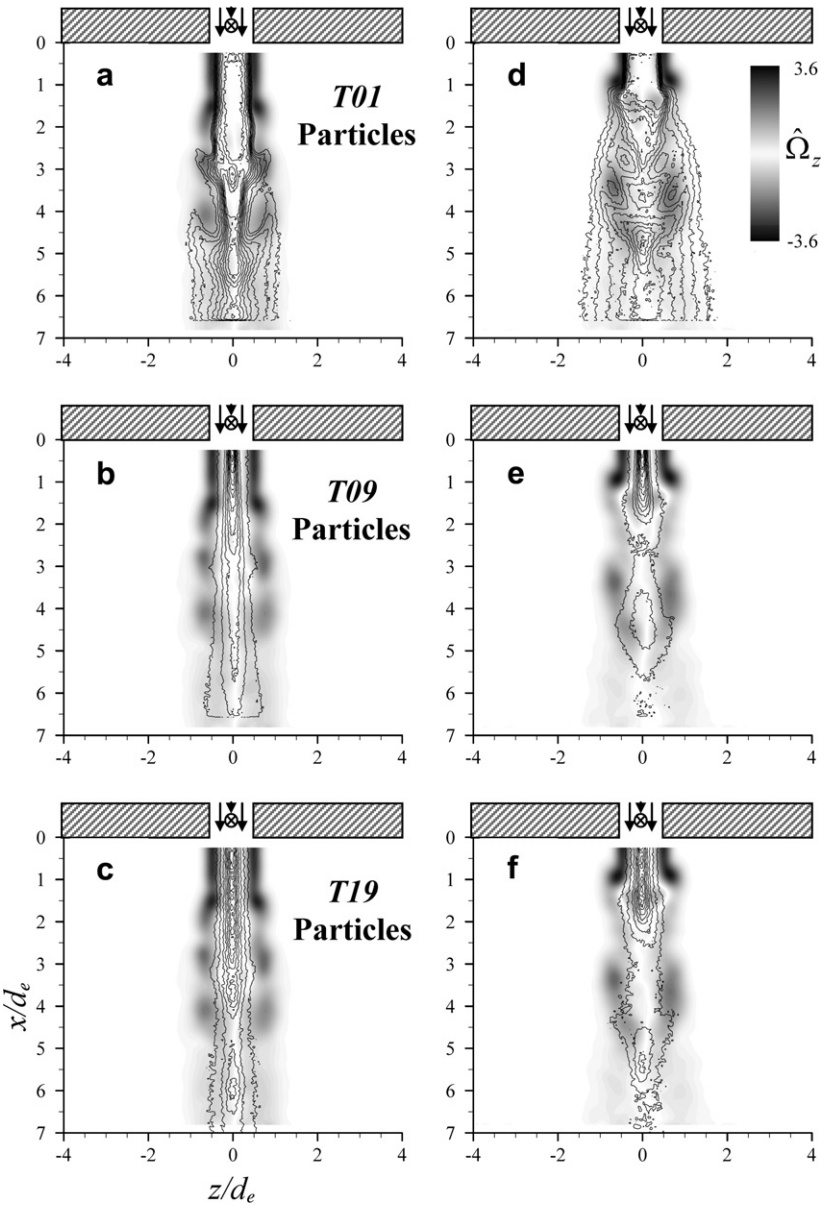

Fig. 14. Phase-averaged ($\phi = 180°$) normalized particle number density distributions (lines) superimposed on the corresponding single-phase vorticity fields (floods) with $C_\mu = 0.005$ (a–c) and 0.16 (d–f) for the *T*01(a, d), *T*09(b, e), and *T*19 (c, f) particles in the x–z centerline plane.

presents the phase-averaged ($\phi = 180°$) particle velocity vector field superimposed onto the carrier fluid vortical structures along the x–y centerline plane with $C_\mu = 0.005$ (Fig. 15a–c) and 0.16 (Fig. 15d–f) for the *T*01 (Fig. 15a and d), *T*09 (Fig. 15b and e), and *T*19 (Fig. 15c and f) particles. In order to accurately explore the effect of the vortical structures on the particles, a zoomed-in view is presented as marked by the dashed line in Fig. 13.

With the synthetic jet activated at $C_\mu = 0.005$, the *T01* particles (Fig. 15a) near the vortical structures are pulled away from the main jet centerline toward the vortical structures. The *T01* particles within the potential core are advected straight downstream (along the x-axis) for $x/d_e < 2$ where the particles have their highest concentration (refer to Fig. 9f), while those closest to the vortical structures are drawn away from the potential core. By contrast, the *T*09 and *T*19 particles (Fig. 15b and c, respectively) remain along the main jet centerline throughout the measurement plane.

When the synthetic jet is activated at $C_\mu = 0.16$ (Fig. 15d, e, and f; *T*01, *T*09, and *T*19 particles, respectively), the particles surrounding the vortical structures are accelerated away from the structures with higher velocities for each of the particle classes. Some of the particles are not expelled from the vortices but, instead, reverse direction and are advected around the vortices (at very low velocity). This result is expected for the *T*01 particles (Fig. 15d), which has a low Stokes number, but was somewhat unexpected for the *T*09 and *T*19 particles (Fig. 15e and f, respectively), which have Stokes numbers that are much larger than unity. The authors attribute this to the high amplitude forcing of the $C_\mu = 0.16$ synthetic jet that creates large vortical structures with magnitudes that are large enough to influence even these high Stokes number particles. This is in contrast to much of the literature (Longmire and Eaton, 1992; Eaton and Fessler, 1994; and others) that use low amplitude acoustic forcing to influence the high Stokes number particles, which are not appreciably influenced by the forcing and appear more like the $C_\mu = 0.005$ forced particle-laden jets (Fig. 15b and c; *T*09 and *T*19 particles, respectively).

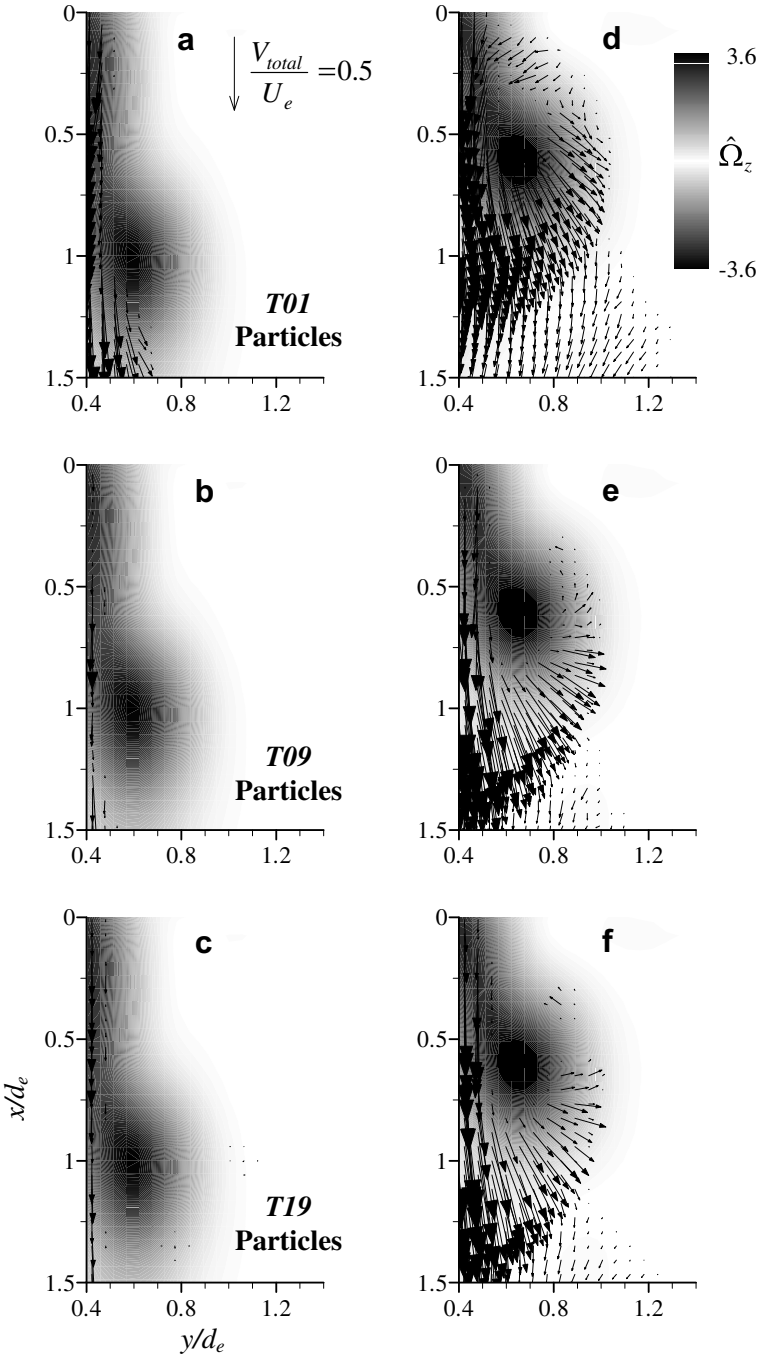

Fig. 15. Zoomed-in phase-averaged ($\phi = 180°$) normalized particle velocity vector fields superimposed on the corresponding single-phase vorticity fields (floods) with $C_\mu = 0.005$ (a–c) and 0.16 (d–f) for the *T*01(a, d), *T*09(b, e), and *T*19 (c, f) particles in the *x*–*y* centerline plane.

3.3. Weighted contributions

As was mentioned above, the synthetic jet affects the particle-laden jet through two mechanisms that are based on altering the drag force produced by the carrier fluid: (1) the synthetic jet's *direct* impulse, which transfers momentum to the fluid around the particles; and (2) *indirect* control via the vortical structures (preferential concentration) that are formed due to the gaseous-phase unstable modes. To further understand the weighted contribution of each mechanism on the particulate phase, the synthetic jet location was moved farther upstream of the main jet exit (i.e., within the main jet nozzle), where the distance between the control jet and the main jet exit is defined as t_c. Tamburello and Amitay (2007b) showed that the effectiveness of altering a single-phase free jet with a single perpendicular synthetic jet actuator was reduced by moving the synthetic jet farther upstream of the main jet exit. It is speculated that by moving the synthetic jet farther upstream into the main jet nozzle, the effects of the synthetic jet's impulse is reduced and the primary effect becomes the growth of the naturally unstable modes, which is also reduced but to a lesser extent. This has to be validated using numerical simulation, which is out of the scope of this paper. In terms of a particle-laden jet, these results suggest that the indirect effect on the particulate phase will be slightly reduced but the direct effects will be significantly

mitigated. Therefore, the effect of the synthetic jet's upstream location on the *T*09 particle-laden jet was also investigated and is discussed in this section.

Fig. 16 presents the normalized streamwise (Fig. 16a–c and g–i), cross-stream (Fig. 16d–f), and spanwise (Fig. 16j–l) particle velocity profiles in the *x*–*y* (Fig. 16a–f) and *x*–*z* (Fig. 16g–l) centerline planes for the forced jet with $C_\mu = 0.16$ for $t_c/d_e = 0.4$, 0.9, and 1.4 at $x/d_e = 1$ (Fig. 16a, d, g and j), 3 (Fig. 16b, e, h and k), and 6 (Fig. 16c, f, i and l). Without flow control, the normalized streamwise velocity distributions are symmetric about the *x*-axis, where the peak velocity decreases and jet width increase with downstream distance. At $x/d_e = 1$, the velocity profile has a double-peak distribution that flattens out by $x/d_e = 3$ and becomes rounded by the end of the measurement plane ($x/d_e = 6$).

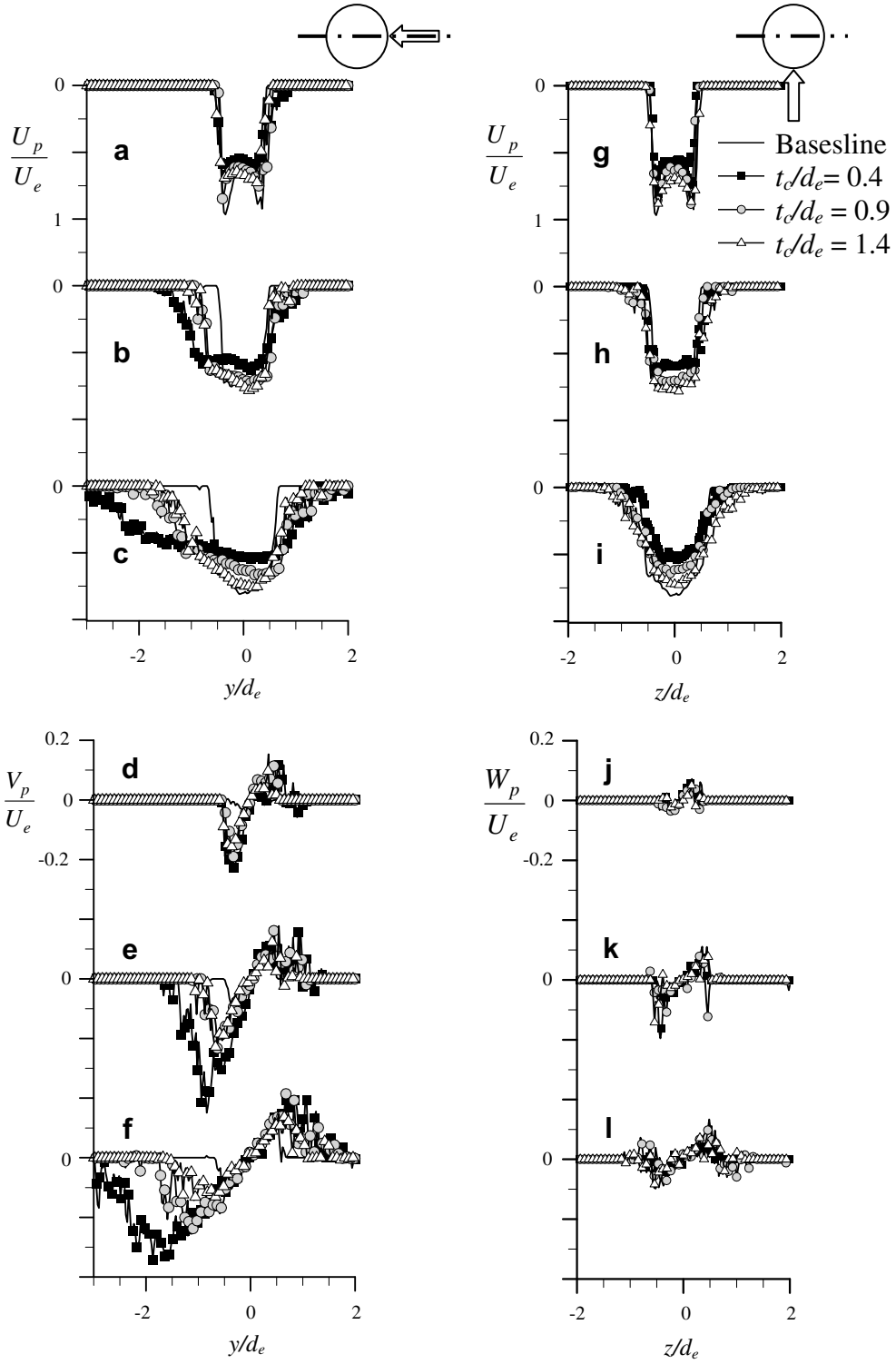

Fig. 16. Normalized streamwise (a–c, g–i), cross-stream (d–f), and spanwise (j–l) velocity profiles at different t_c/d_e with $C_\mu = 0.16$ for the *T*09particles at $x/d_e = 1$ (a, d, g, j), 3 (b, e, h, k), and 6 (c, f, i, l) in the *x*–*y* (a–f) and *x*–*z* (g–l) centerline planes.

When the synthetic jet is activated, the synthetic jet located at $t_c/d_e = 0.4$ has the largest cross-stream U_p/U_e profiles (x–y centerline planes, for $x/d_e = 3$ and 6, Fig. 14b and c, respectively) and the smallest peak velocity magnitudes (throughout the measurement plane) compared to the other two synthetic jet locations. By contrast, the synthetic jet located at $t_c/d_e = 1.4$ yields the smallest changes from the baseline with the most narrow velocity profiles. Note that the largest differences between the three synthetic jet locations are on the side away from the control, which can be attributed to the mitigation of the direct effect.

In the x–z measurement plane (Fig 16g–i), the U_p/U_e profiles remain relatively symmetric about the x-axis with double-peak distributions at $x/d_e = 1$ (Fig 16g). The synthetic jet located at $t_c/d_e = 1.4$ yields the highest velocities magnitudes and the widest

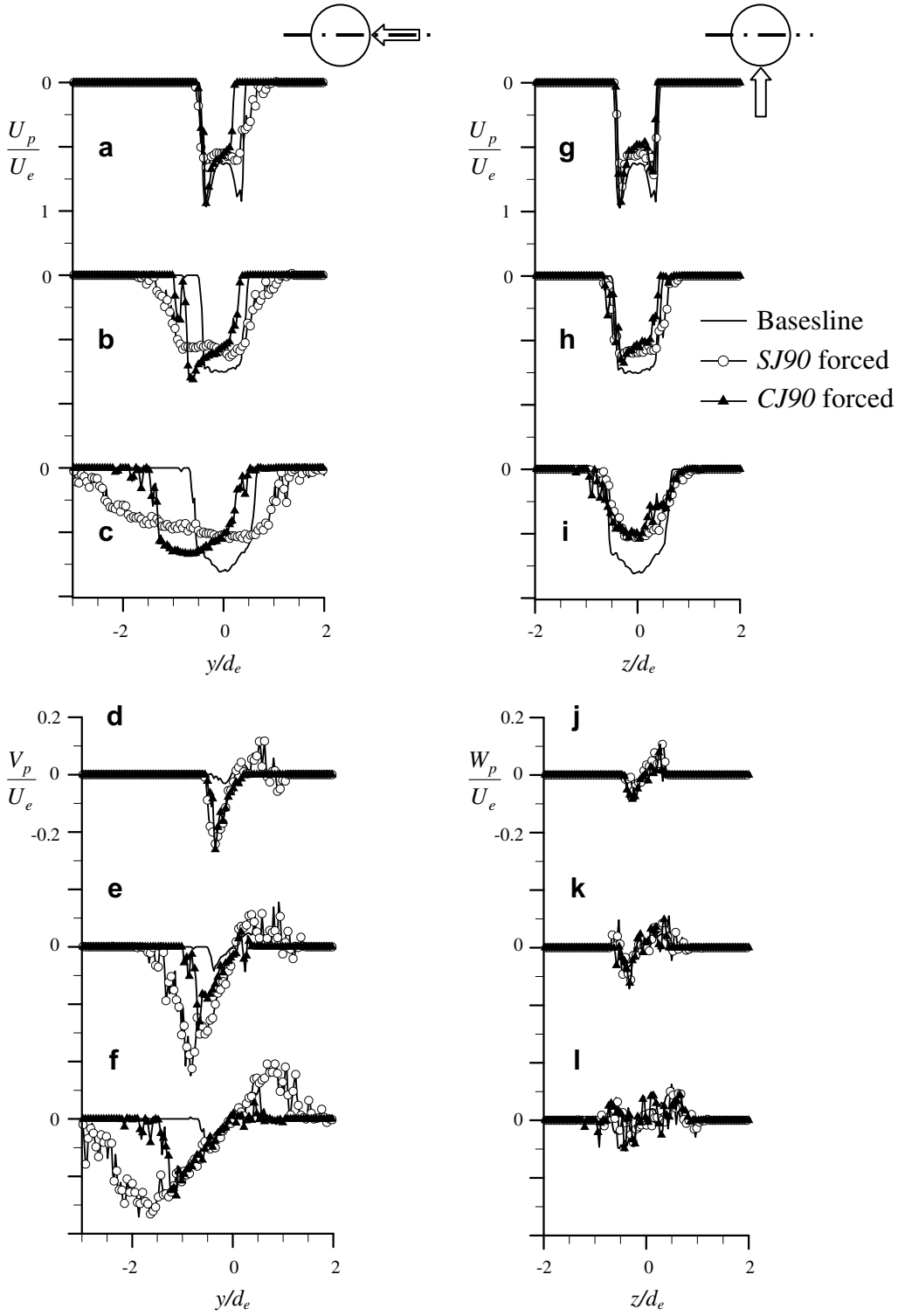

Fig. 17. Normalized streamwise (a–c, g–i), cross-stream (d–f), and spanwise (j–l) velocity profiles for the *SJ90* and *CJ90* forced jets with $C_\mu = 0.16$ for the *T*09particles at $x/d_e = 1$ (a, d, g, j), 3 (b, e, h, k), and 6 (c, f, i, l) in the x–y (a–f) and x–z (g–l) centerline planes.

spanwise extent throughout the measurement domain, which can be attributed to the vectoring of the other two cases ($t_c/d_e = 0.4$ and 0.9) out of the measurement plane to a greater extent.

Next, the normalized cross-stream (x–y centerline plane, Fig 16d–f) and spanwise (x–z centerline plane, Fig. 16j–l) velocity profiles are examined. The normalized cross-stream and spanwise velocity profiles for the baseline jet are anti-symmetric with a negative peak on the left side and a positive peak on the right side, which is indicative of increased spreading in both directions. When the synthetic jet is activated, the cross-stream and spanwise extents of the velocity profiles increase for all synthetic jet locations, especially in the x–y centerline plane (Fig. 16d–f) on the side opposite the synthetic jet. In this plane, the synthetic jet located closest to the main jet exit ($t_c/d_e = 0.4$) yields larger effects than the other two synthetic jet locations, especially on the side away from the control. In addition, the negative V_p/U_e (side opposite the synthetic jet) has higher magnitudes than the positive V_p/U_e due to the increased spreading. In the x–z centerline plane (Fig. 16j–l), the activation of the synthetic jets at each upstream location results in increased spanwise extents. Note that similar results were shown at lower momentum coefficients, but are not shown for the sake of brevity.

To further understand the effect of each mechanism on the particulate phase, the effect of the synthetic jet (*SJ90*) on the *T*09 particle-laden jet is compared to that of a continuous control jet (*CJ90*) where the only control mechanism is due to the direct effects of the impulse. Both control jets are issued within the main jet nozzle at $t_c/d_e = 0.4$ with $C_\mu = 0.16$.

Fig. 17 presents the normalized streamwise (Fig. 17a–c and g–i), cross-stream (Fig. 17d–f), and spanwise (Fig. 17j–l) particle velocity profiles in the x–y (Fig. 17a–f) and x–z (Fig. 17g–l) centerline planes for the forced jet with $C_\mu = 0.16$ at $x/d_e = 1$ (Fig. 17a, d, g and j), 3 (Fig. 17b, e, h and k), and 6 (Fig. 17c, f, i and l).

When the synthetic jet is activated, the cross-stream extent of the streamwise particle velocity (in the x–y plane, Fig. 17a–c) is increased in both directions throughout the measurement plane. In addition, the peak velocities decrease (compared to the baseline) with downstream distance. By contrast, the continuous control jet yields a decrease (compared to the baseline) in the cross-stream extent for $x/d_e = 1$ (Fig. 17a), while the velocity distribution is wider than the baseline farther downstream ($x/d_e = 3$ and 6, Fig. 17b and c, respectively). The *CJ90* also results in higher peak velocities (than the synthetic jet) that are vectored farther away from the control jet with downstream distance. Furthermore, as the downstream distance increases, the synthetic jet yields a larger vectoring to the side away from the control due do the additional spreading resulting from the amplification of the coherent structures. These differences can be attributed to the continuous control jet's lack of *indirect* effects. Since the continuous control jet momentum is used to directly influence the particles, they are only forced away from the continuous control jet side.

In the x–z centerline plane (Fig. 17g–i) when either control jet is activated, the normalized streamwise velocity profiles are relatively symmetric about the x-axis throughout the flow field. However, the peak velocity is reduced due to the vectoring of the particles off of the measurement plane.

In the x–y centerline plane, the magnitudes and cross-stream extent of the V_p/U_e profiles (Fig. 17d–f) increase (compared to the baseline) for both control jets throughout the measurement plane, especially on the side opposite the control jet, which is indicative of increased spreading. In addition, when the synthetic jet is used, larger effects (compared with the continuous control jet cases) are shown on both sides of the main jet. Note that the continuous control jet case has small cross-stream velocity on the control jet side and its highest V_p/U_e magnitudes are on the side opposite the control jet due to the large vectoring of the particles away from the continuous control jet.

In the x–z centerline plane (Fig. 17j–l), both flow control techniques yield slightly increased spreading of the particle-laden jet throughout the measurement domain, with relatively equal peak spanwise particle velocities for both the *SJ90* and *CJ90* cases.

4. Conclusions

This paper examines experimentally the effects of flow control on an axisymmetric particle-laden jet via a single synthetic jet actuator that is issued perpendicular to the main jet, within the main jet nozzle. This work provides an insight into the direct and indirect mechanisms of flow control and their effect on the complex three-dimensional flow field resulting from the interaction by utilizing a three-dimensional rendering technique based on multiple two-dimensional measurement planes. The synthetic jet was driven at a frequency of 1000 Hz ($St_r = 0.16$), which corresponds to the naturally unstable modes of the carrier fluid and, thus, takes advantage of the naturally amplifying structures within the main jet flow to better influence the particulate phase.

The effect of the synthetic jet on the particle velocity and distribution is through both *direct* and *indirect* mechanisms. The particle-laden jet was directly affected by the addition of momentum from the control jet and indirectly, through preferential concentration, by controlling the size and location of the coherent vortical structures downstream of the main jet exit. When the synthetic jet was activated, its impulse penetrated into the particle-laden jet such that the carrier fluid drags the particles away from the synthetic jet side (i.e., *direct* effect). The synthetic jet also formed large coherent vortical structures in the carrier fluid that *indirectly* affected particle spreading, as well as the mean and RMS velocity fields, throughout the measurement domain. When the synthetic jet was activated farther upstream (within the main jet nozzle), particle spreading was reduced, as was also shown in previous work for the single-phase jet.

When a continuous control jet was used (instead of the synthetic jet), the effect was only to vector the particles away from the control due to the lack of the *indirect* mechanism. Since the entire momentum from the continuous control jet is used to *directly* influence the particulate phase, relatively all of the particles are forced away from the continuous jet side.

The effect of the Stokes number was also examined where, for each of the particle sizes tested, the particles were shown to be influenced by the control. The lowest Stokes number particles ($St^*_{f,25m/s} = 0.703$) followed the gaseous phase fairly well, with velocity distributions that were similar to the single-phase flow. The higher Stokes number particles, which are an order of magnitude larger ($St^*_{f,25m/s} = 4.72$ and 9.31), were less responsive to the gaseous phase. However, when high-amplitude forcing was used, large vortical structures with magnitudes that are large enough to influence these high Stokes number particles and advected some of the particles around the vortices (at a very low velocity) rather than expelling them. This suggests that preferential concentration depends on both the Stokes number as well as the strength of the coherent vortical structures.

Acknowledgement

This work has been supported by RPI's internal funding.

References

Amitay, M., Cannelle, F., 2006. Evolution of Finite Span Synthetic Jets. Phys. Fluids 18, 054101 (16 pages).

Amitay, M., Kondor, S., Herdic, S., Anderson, S.L., 2003. Directed particle-laden micro-jet for dental caries evacuation. FEDSM2003 – 45059.
Anderson, S.L., 1997. Particle motions in the stagnation region of natural and forced impinging round air jets. Doctoral Thesis, University of Minnesota.
Anderson, S.L., Longmire, E.K., 1995. Particle motion in the stagnation zone of an impinging air jet. J. Fluid Mech. 299, 333–366.
Apte, S.V., Mahesh, K., Moin, P., Oefelein, J.C., 2003. Large-eddy simulation of swirling particle-laden flows in a coaxial-jet combustor. Int. J. Multiphase Flow 29, 1311–1331.
Bulzan, D.L., Shuen, J.-S., Faeth, G.M., 1987. Particle-laden swirling free jets: Measurements and predictions. AIAA Paper 87 – 0303.
Cannelle, F., Amitay, M., 2005. Synthetic jets: Spatial evolution and transitory behavior. AIAA Paper 2005 – 0102.
Cerecedo, L.M., Aisa, L., Garcia, J.A., Santolaya, J.L., 2004. Changes in a coflowing jet structure caused by acoustic forcing. Exp. Fluids 36, 867–878.
Eaton, J.K., Fessler, J.R., 1994. Preferential concentration of particles by turbulence. Int. J. Multiphase Flow 20, 169–209.
Fessler, J.R., Kulick, J.D., Eaton, J.K., 1994. Preferential concentration of heavy particles in a turbulent channel flow. Phys. Fluids 6, 3742–3749.
Fessler, J.R., Eaton, J.K., 1997. Particle response in a planar sudden expansion flow. Exp. Therm. Fluid Sci. 15, 413–423.
Glezer, A., Amitay, M., 2002. Synthetic jets. Ann. Rev. Fluid Mech. 34, 503–529.
Hardalupas, Y., Taylor, A.M.K.P., Whitelaw, J.H., 1989. Velocity and particle-flux characteristics of turbulent particle-laden jets. Proc. Roy. Soc. Lond. A 426, 31–78.
Hassan, Y.A., Blanchat, T.K., Seeley Jr., C.H., Canaan, R.E., 1992. Simultaneous velocity measurement of both components of a two-phase flow using particle image velocimetry. Int. J. Multiphase Flow 18, 371–395.
Hetsroni, G., 1989. Particle-turbulence interaction. Int. J. Multiphase Flow 15, 735–746.
Hoffmann, R., Moreira, A.L.N., 1996. Particle dispersion in an acoustically excited round jet. In: 8th International Symposium on Applications of Laser Techniques to Fluid Mechanics, Lisbon, Portugal.
Kiger, K.T., Lasheras, J.C., 1995. The effect of vortex pairing on particle dispersion and kinetic energy transfer in a two-phase turbulent shear layer. J. Fluid Mech. 302, 149–178.
Longmire, E.K., Eaton, J.K., 1992. Structure of a particle-laden round jet. J. Fluid Mech. 236, 217–257.
Longmire, E.K., Eaton, J.K., 1994. Active open-loop control of particle dispersion in round jets. AIAA J. 32, 555–563.
Middha, P., Wexler, A.S., 2003. Particle focusing characteristics of sonic jets. Aero. Sci. Technol. 37, 907–915.
Pothos, S., 2002. Control of particles and turbulence using a piezoelectric actuator. Doctoral Thesis, University of Minnesota.
Pothos, S., Longmire, E.K., 2002. Control of a particle-laden jet using a piezo-electric actuator. In: 11th International Symposium on Applications of Laser Techniques to Fluid Mechanics, Lisbon, July 2002.
Prevost, F., Boree, J., Nuglisch, H.J., Charnay, G., 1996. Measurements of fluid/particle correlated motion in the far field of an axisymmetric jet. Int. J. Multiphase Flow 22, 685–701.
Saffman, P.G., 1962. On the stability of laminar flow of a dusty gas. J. Fluid Mech. 13, 120–128.
Sakakibara, J., Wicker, R.B., Eaton, J.K., 1996. Measurements of the particle-fluid velocity correlation and the extra dissipation in a round jet. Int. J. Multiphase Flow 22, 863–881.
Sakakibara, K., Hishida, K., Phillips, W.R.C., 2001. On the vortical structure in a plane impinging jet. J. Fluid Mech. 434, 273–300.
Schabacker, J., Bölcs, A., 1996. Investigation of turbulent flow by means of the PIV method. In: 13th Symposium on Measuring Techniques for Transonic and Supersonic Flows in Cascades and Turbomachines, Zurich, Switzerland. September 5–6, 1996.
Smith, B.L., Glezer, A., 1998. The formation and evolution of synthetic jets. Phys. Fluids 10, 2281–2297.
Smith, B.L., Glezer, A., 2002. Jet vectoring using synthetic jets. J. Fluid Mech. 458, 1–34.
Squires, K.D., Eaton, J.K., 1990. Particle response and turbulence modification in isotropic turbulence. Phys. Fluids 2, 1191–1203.
Squires, K.D., Eaton, J.K., 1991. Preferential concentration of particles by turbulence. Phys. Fluids 3, 1169–1178.
Tamburello, D.A., 2007. Active flow control of axisymmetric single-phase and particle-laden jets. Doctoral Thesis, Rensselaer Polytechnic Institute.
Tamburello, D.A., Amitay, M., 2007a. Interaction of a free jet with a perpendicular control jet. J. Turbul. 8, 1–27.
Tamburello, D.A., Amitay, M., 2007b. Three-dimensional interactions of a free jet with a perpendicular synthetic jet. J. Turbul. 8, 1–21.
Tamburello, D.A., Amitay, M., 2007c. Dynamic response of a free jet following the activation of a single synthetic jet. J. Turbul. 8, 1–19.
Tamburello, D.A., Amitay, M., in press. Active control of a free jet using a synthetic jet. Int. J. Heat Fluid Flow.
Torobin, L.B., Gauvin, W.H., 1959. Fundamental aspects of solids/gas flow. Part I: Introductory concepts and idealized sphere motion in viscous regime. Canad. J. Chem. Eng. 37, 129–141.
Wicker, R.B., Eaton, J.K., 1999. Effect of injected longitudinal vorticity on particle dispersion in a swirling, coaxial jet. J. Fluids Eng. 121, 766–772.
Wicker, R.B., Eaton, J.K., 2001. Structure of a swirling, recirculating coaxial free jet and its effect on particle motion. Int. J. Multiphase Flow 27, 949–970.
Winkler, C.M., Rani, S.L., Vanka, S.P., 2004. Preferential concentration of particles in a fully developed turbulent square duct flow. Int. J. Multiphase Flow 30, 27–50.
Wood, A.M., Hwang, W., Eaton, J.K., 2005. Preferential concentration of particles in homogenous and isotropic turbulence. Int. J. Multiphase Flow 31, 1220–1230.
Yang, Y., Crowe, C.T., Chung, J.N., Troutt, T.R., 2000. Experiments on particle dispersion in a plane wake. Int. J. Multiphase Flow 26, 1583–1607.
Yu, Y., Zhou, L.X., Zheng, C.G., Liu, Z.H., 2003. Simulation of swirling gas-particle flows using different time scales for the closure of two-phase velocity correlation in the second-order moment two-phase turbulence model. J. Fluids Eng. 125, 247–250.
Yu, K.F., Lau, K.S., Chan, C.K., 2004. Numerical simulation of gas-particle flow in a single-side backward-facing step flow. J. Comput. Appl. Math. 163, 319–331.
Yule, A.J., 1978. Large-scale structure in the mixing layer of a round jet. J. Fluid Mech. 89, 413–432.